Aalto University

School of Science and Technology

Faculty of Information and Natural Sciences

Visa Vesterinen

# Optimization of a Metallic Thermoacoustic Sound Source

Master´s thesis submitted in partial fulfillment of the requirements for the degree of Master of Science in Technology in the Degree Programme in Engineering Physics and Mathematics.

Espoo, November 29, 2010

Supervisor: Prof. Esko I. Kauppinen

Instructor: Dr. Juha Hassel

| Aalto University<br>School of Science and Technology<br>Faculty of Information and Natural Sciences | ABSTRACT OF THE MASTER'S THESIS |
| --- | --- |
| Author: Visa Vesterinen | |
| Title: Optimization of a Metallic Thermoacoustic Sound Source | |
| Title in Finnish:  Metallisen termoakustisen äänilähteen optimointi | |
| Degree Programme: Degree Programme in Engineering Physics and Mathematics | |
| Major subject: Engineering Physics | Minor subject: Mathematics |
| Chair (code): Tfy-3 Physics | |
| Supervisor: Prof. Esko I. Kauppinen | Instructor: Dr. Juha Hassel |

Abstract:

Propagation of sound in fluids is regarded only as an isentropic process in traditional applications, but the underlying theory of fluid dynamics and thermodynamics gives rise to interesting phenomena in specialized conditions. Thermoacoustic coupling is a weak, localized process which can be used to drive thermal engines with acoustic power. In the inverse situation, thermal energy can be converted into sound and even ultrasound. In this work, theoretical foundations of thermoacoustic loudspeakers are reviewed. Coupling of temperature and pressure in fluids can be explained with two partial differential equations. By solving thermoacoustic fields analytically and numerically, the performance of various loudspeaker designs can be studied. Theory is compared to experiments with the aid of suspended metal wire array loudspeakers manufactured by VTT Technical Research Centre of Finland. It is essential to understand the interplay between frequency-dependent factors that limit acoustic performance. In the search for the ultimate limit of loudspeaker efficiency, it can be justified that the upper bounds are determined by loudspeaker size and the parameters of the fluid which control thermoacoustic coupling strength. Several optimization steps are proposed for improving the metal wire array loudspeakers.

| Date: 29.11.2010 | Language:  English | Number of pages:<br>46+5 |
| --- | --- | --- |

| Aalto-yliopisto<br>Teknillinen korkeakoulu<br>Informaatio- ja luonnontieteiden tiedekunta | DIPLOMITYÖN TIIVISTELMÄ |
|---|---|

Tekijä: Visa Vesterinen

Työn nimi: Metallisen termoakustisen äänilähteen optimointi

Title in English: Optimization of a Metallic Thermoacoustic Sound Source

Tutkinto-ohjelma: Teknillisen fysiikan ja matematiikan tutkinto-ohjelma

| Pääaine:  Teknillinen fysiikka | Sivuaine: Matematiikka |
|---|---|

Opetusyksikön (ent. professuuri) koodi: Tfy-3 Fysiikka

| Työn valvoja: Prof. Esko I. Kauppinen | Työn ohjaaja(t): TkT Juha Hassel |
|---|---|

Tiivistelmä:

Äänen etenemistä kaasussa, kuten esimerkiksi ilmassa, käsitellään perinteisesti isentrooppisena ilmiönä. Teoria virtaus- ja termodynamiikasta on kuitenkin monipuolinen ja sen avulla voidaan ymmärtää mielenkiintoisia ilmiöitä, jotka näkyvät vain erikoistilanteissa. Näistä ilmiöistä yksi on termoakustinen kytkeytyminen, joka sitoo paine- ja lämpötilakentät heikosti yhteen. Lämpövoimakoneita voidaan ajaa termoakustisesti käyttämällä ääniaaltoja teholähteenä. Kääntäen on mahdollista tuottaa lämpöenergiasta ääntä sekä ihmisten kuulemilla taajuuksilla että ultraäänitaajuuksilla. Tässä diplomityössä selitetään teoreettisesti, miten termoakustiset kaiuttimet toimivat. Äänen ja lämpötilan oskillaatioita kuvataan kahdella toisiinsa kytkeytyneellä osittaisdifferentiaaliyhtälöllä. Kaiuttimien suorituskykyä tutkitaan ratkaisemalla ilman paine- ja lämpötilakentät analyyttisesti ja numeerisesti. Tuloksia vertaillaan akustisiin mittauksiin, joissa termoakustisina äänilähteinä toimivat ripustettujen metallilankojen muodostamat hilat. Lankahilat on suunniteltu ja valmistettu Valtion teknillisessä tutkimuskeskuksessa (VTT). Kaiutinanalyysissä selvitetään, miten suorituskykyä eli hyötysuhdetta vähentävät, taajuudesta riippuvat tekijät suhtautuvat toisiinsa. Työssä löydetään termoakustisen kaiuttimen hyötysuhteen yläraja, johon vaikuttavat ainoastaan kaiuttimen koko ja kaiutinta ympäröivän ilman termofysikaaliset ominaisuudet. Lisäksi pohditaan lankahilakaiuttimien optimoimista monelta kantilta.

| Päivämäärä: 29.11.2010 | Kieli: englanti | Sivumäärä: 46+5 |
|---|---|---|

Avainsanat: sovellettu fysiikka; termoakustiikka; äänilähde; ripustettu metallilanka; taajuusvaste; akustinen hyötysuhde; ultraääni

## Preface

This Master's thesis was written during an internship at VTT Technical Research Centre of Finland. I was introduced to the topic of thermoacoustics by Quantronics team in May 2009. My work deals with thermoacoustically operated metal wire arrays that were designed and manufactured at VTT. The research problem on which I primarily focused was to develop computational methods to explain loudspeaker characteristics. Eventually, the work expanded into the fields of acoustic measurements and analytic Green's functions. I would like to thank my instructor Juha Hassel for his continuous support. I had plenty of stimulating discussions with him, Antti Niskanen and Panu Helistö. Support from the Academy of Finland is acknowledged as well as the generous computing resources of CSC, the Finnish IT Center for Science.

Espoo, November 29, 2010

Visa Vesterinen

# Contents

# Abbreviations

CNT    Carbon nanotube
FFT    Fast Fourier transform
FD     Finite difference
FR     Frequency response
FEM    Finite element method
IR      Impulse response
MLS    Maximum length sequence
PDE    Partial differential equation
RMS    Root mean squared
SNR    Signal-to-noise ratio
SPL    Sound pressure level

# 1 Introduction

Thermoacoustic excitation of sound is a process where short-ranged thermal waves are emitted from a solid, resistive material which is heated periodically with electric Joule power. Pressure waves are excited when the thermal waves make air contract and expand periodically in the vicinity of the resistor. The audible sounds that we are able to perceive are basically oscillations of pressure and fluid velocity that occur in phase. However, these oscillations have usually small amplitudes which means that Navier-Stokes-Fourier equations can be linearized in air. Perturbative fields of temperature and pressure can thus be solved from a pair of coupled partial differential equations.

Demonstrated in the end of 19th century, the first thermoacoustic emitters were thin metallic films driven with AC electric signals, and it was realized that excited root mean square pressure follows a power law $P_{\mathrm{rms}} \propto f^{1/2}/C_s$ where $f$ is sound frequency and $C_s$ is heat capacity per unit area of film [1]. The major drawback of the devices was that efficiency was greatly limited by $C_s$ even if the films were only a few micrometres thick. This problem wasn't cured until recently when carbon nanotube films were utilized thermoacoustically [2, 3, 4]. Soon after that, metallic loudspeakers with similarly good performance were designed at VTT Technical Research Center of Finland. Integrated directly into a silicon wafer, the loudspeakers consist of regular, suspended arrays of nanometre-thick aluminium wires.

This work focuses on studying the properties of VTT loudspeakers. In the experimental part acoustical measurements are performed. Sound pressure level (SPL) and the shape of radiation pattern are measured as a function of frequency and input electric power. Power law behaviour $P_{\mathrm{rms}} \propto f^p$ is searched for in frequency responses, and with sufficient knowledge on radiation patterns acoustic output power can be estimated. The purpose of the computational part of this work is to develop a simulation model which can explain the acoustic behaviour of suspended metal wire arrays. With the aid of a workable linear model the parameters of the array can be optimized. In addition, the existence and properties of a thermoacoustic upper bound of loudspeaker efficiency are discussed. The measured efficiency of VTT loudspeakers can be directly compared to the upper limit in question.

## 2  Theoretical background

### 2.1  Linear thermoacoustics

In linearized theory of acoustics all relevant physical quantities such as pressure, density, entropy and temperature have ambient values denoted with subscript zero. As a result of thermoacoustic excitation of sound, the corresponding scalar and vector fields in air are slightly perturbed from the ambient situation. Linear thermoacoustics can be described with two partial differential equations (PDEs): a diffusion equation of temperature field $T$ and a wave equation of pressure field $P$ [5]. Using linearized Navier-Stokes-Fourier theory as a starting point, these equations can be easily derived in a non-viscous situation [6] (for a detailed version in Finnish, see special assignment [7]). The breakdown of non-viscosity at high frequencies will be discussed later. The time derivative of pressure acts as a source in the diffusion equation:

$$\nabla^2 T - \frac{1}{\alpha}\frac{\partial T}{\partial t} = -\frac{S}{\kappa} - \frac{1}{\kappa}\frac{\partial P}{\partial t}, \tag{1}$$

where $\alpha$ is diffusion constant of air, $\kappa$ is heat conductivity of air and $S$ is an arbitrary heat source in units W/m$^3$. The second time derivative of temperature is a source of pressure in the isothermal wave equation:

$$\nabla^2 P - \frac{1}{c_T^2}\frac{\partial^2 P}{\partial t^2} = -\frac{\rho_0}{T_0}\frac{\partial^2 T}{\partial t^2}, \tag{2}$$

where $c_T$, $\rho_0$ and $T_0$ are isothermal speed of sound, density of air, and ambient (room) temperature of air. Isentropic speed of sound $c_0$ can be solved from

$$\frac{1}{c_0^2} = \frac{1}{c_T^2} - \frac{1}{T_0 c_P}, \tag{3}$$

where specific heat in constant pressure is $c_P = \kappa/(\alpha\rho_0)$. The diffusion equation (1) can be differentiated with respect to time and then plugged into the wave equation (2):

$$\nabla^2 P - \frac{1}{c_0^2}\frac{\partial^2 P}{\partial t^2} = -\frac{\alpha\rho_0}{\kappa T_0}\frac{\partial(\kappa\nabla^2 T + S)}{\partial t} = -\frac{1}{T_0 c_P}\frac{\partial h}{\partial t}. \tag{4}$$

In this isentropic wave equation $h$ is used to denote the heat added per unit time and volume.

## 2.2 Periodic heating

Heat generated in a conductor due to resistance is characterized by Joule's law

$$P_J = \frac{(V_{\mathrm{dc}} + V_{\mathrm{ac}}\sin(2\pi f_0 t))^2}{R} \tag{5}$$

where $V_{\mathrm{dc}}$ and $V_{\mathrm{ac}}$ are DC and AC components of voltage amplitudes and $R$ is the resistance. The frequency of AC voltage is $f_0$. Expanding the square of voltage results in a stationary term (average electric power $\bar{P}_J$) and two sinusoidal terms with frequencies $f_0$ and $2f_0$. What happens to the generated heat can be described with energy balance on the resistor-air interface:

$$P_J = AC_s\frac{\partial T}{\partial t} - A\kappa\frac{\partial T}{\partial n} + A\beta_0 T. \tag{6}$$

Here $A$ and $C_s$ are the area and heat capacity per unit area of the resistor. $AC_s\dot{T}$ represents the capability of storing and releasing heat; time derivatives are marked with dots starting from now. The second term $-A\kappa\frac{\partial T}{\partial n}$ provides heat conduction according to Fourier's law: $\frac{\partial}{\partial n}$ is the derivative in the direction of outer normal vector. Finally, $A\beta_0 T$ is responsible for all the remaining loss mechanisms such as radiation: $\beta_0$ is the symbol for rate of heat loss per unit area and unit rise in temperature. Typically, the energy balance (6) is regarded as a thermal boundary condition in PDEs (1) and (4). [2]

Driving a conductor with voltage $V_{\mathrm{ac}}$ (plus optionally $V_{\mathrm{dc}}$) leads to oscillatory perturbations of temperature and pressure fields in the resistor's surroundings. Thermoacoustic effect is primarily responsible for emission of sound at doubled frequency $2f_0$, there will be no $f_0$ component unless the DC bias is switched on. It should be also noted that resistance $R$ can depend on temperature: especially at high AC input power the internal temperature of the loudspeaker oscillates so much that additional acoustic $3f_0$ and $4f_0$ emissions can be detected [3]. Throughout this work, however, no DC bias is applied and the resistance nonlinearity is neglected altogether. Thermal and sound oscillations can thus occur only at frequency $2f_0$.

Periodic heating at the interface excites exponentially decaying temperature waves. If allowed to propagate through air, a portion of the waves is converted into sound. The temperature waves, whose range can be estimated to be one thermal wavelength $\lambda_T = 2\pi/k_T = 2\pi\sqrt{\alpha/\omega}$, can be plugged into the partial differential equation (4) to verify that pressure waves are excited from the thin slab of air next to the interface [1]. Angular frequency is denoted here with $\omega = 2\pi f_0$. When the distance from heat sources is large the pressure waves are found to propagate with velocity $c_0$ which corresponds to

3

isentropic wavelength $\lambda_0 = 2\pi/k_0 = \pi c_0/\omega$. The root mean squared pressure can be converted to sound pressure level (SPL) which has logarithmic decibel (dB) units:

$$SPL = 20\log_{10}\left(\frac{P_{\text{rms}}}{P_0}\right)\text{dB},\ P_0 = 20\cdot 10^{-6}\text{ Pa rms.} \tag{7}$$

The rms value of pressure is pressure amplitude multiplied by $1/\sqrt{2}$.

## 2.3  Acoustic power in free field

The acoustic energy density $w$ is composed of kinetic and potential energy densities:

$$w = \frac{\rho_0 v^2}{2} + \frac{P^2}{2\rho_0 c_0^2} \tag{8}$$

in which $v^2$ is the squared amplitude of particle velocity $\vec{v}$. The potential energy describes compression of air. When an arbitrary single-frequency sound source is located at the origin of spherical coordinate system $(r_0, \varphi, \theta)$, the far-field pressure solution becomes a spherical wave equipped with directivity function $F$:

$$P(r, \varphi, \theta) = F(\varphi, \theta)\frac{e^{ik_0 r_0}}{r_0}e^{-2i\omega t}. \tag{9}$$

The time-averaged intensity is defined as

$$I_{av} = \frac{1}{2}\text{Re}\{P^* v\}. \tag{10}$$

After eliminating velocity with Euler equation

$$\rho_0\dot{\vec{v}} = -\nabla P, \tag{11}$$

which gives

$$v = \frac{P}{\rho_0 c_0}\left(1 - \frac{1}{ik_0 r_0}\right) \tag{12}$$

for a spherical wave in large-$r_0$ limit, the intensity is found to depend on the square of rms pressure:

$$I_{av} = \frac{P_{\text{rms}}^2}{\rho_0 c_0}. \tag{13}$$

Average acoustic power $P_{\text{ac}}$ at distance $r_0$ from the source is $I_{av}$ integrated over spherical surface area $4\pi r_0^2$:

$$P_{\text{ac}}(\varphi, \theta) = \frac{1}{2\rho_0 c_0}\int_0^{2\pi}\int_0^{\pi}|F(\varphi, \theta)|^2\sin\theta d\theta d\varphi. \tag{14}$$

In half-space the upper limit of $\theta$ is $\pi/2$, though. $P_{\text{ac}}$ agrees with energy conservation since it doesn't depend on distance $r_0$ [6]. On-axis pressure response $|P(r_0, \theta = 0)| = |F(0,0)|/r_0$ is actually the only set of measurement data which is needed for estimating acoustic power if the angular dependence of directivity $F$ is known.

Directivity characteristics of sound sources depend on geometry since interference of waves emitted from multiple locations determines the radiation pattern. In the case of regular array loudspeakers the inner dimensions aren't usually relevant, but the directivity results from global shape. In this work the focus is on planar sources the subdomains of which operate in phase. Fourier transforming acoustic potentials is a straightforward way to determine directivity of planar pistons [8]. The surface velocity of the pistons is assumed to oscillate in $z$-direction with constant amplitude. The angular part of $F$, which here approaches piston area $A$ times $1/(2\pi)$ on the acoustic axis $\theta = 0$, is

$$D(\theta, \varphi) = a^2 \left( \frac{J_1(k_0 a \sin \theta)}{k_0 a \sin \theta} \right) \tag{15}$$

for a circular piston source of sound with radius $a$ [6]. $J_1$ is a Bessel function of the first kind. If the piston source is a rectangle $L_x \times L_y$,

$$D(\theta, \varphi) = \frac{L_x L_y}{2\pi} \operatorname{sinc}\left( \frac{k_0 L_x}{2} \sin \theta \cos \varphi \right) \operatorname{sinc}\left( \frac{k_0 L_y}{2} \sin \theta \sin \varphi \right). \tag{16}$$

Provided that the half-space on-axis response $|P(0,0)|$ of a regular loudspeaker has been measured at some known distance $r_0$ and the angular part of directivity $D$ has been verified with off-axis interference studies, average acoustic power can finally be calculated:

$$P_{\text{ac}} = \frac{|P(0,0)|^2 r_0^2}{2\rho_0 c_0} \int_0^{2\pi} \int_0^{\pi/2} \left( \frac{2\pi D(\theta, \varphi)}{A} \right)^2 \sin\theta \, d\theta \, d\varphi. \tag{17}$$

5

## 3   Research problem

The suspended metal wire arrays fabricated by VTT Technical Research Center of Finland contain up to hundreds of thousands of aluminium wires [9]. The width of wires is 3 $\mu$m and their thickness is as small as 30 nm. All the wires are aligned in a parallel fashion and they are supported by larger aluminium bars as seen in Figure 1. The suspension of the array is characterized by an air gap separating it from Si substrate. The width of the gap is estimated to be $g = 5$ $\mu$m.



Figure 1: Scanning electron microscope image of a VTT loudspeaker. Larger aluminium crossbars are supporting the sound-emitting wires which form a regular array.

Reference [9] features various experimental results and photolithographic fabrication methods are discussed there, too. For the purpose of this work, properties of four distinct loudspeakers are reviewed next. Speakers A (15000 wires), B (6000 wires) and C (12000 wires) have surface area 1 cm × 0.5 cm and larger speaker E has 233200 wires distributed into a 5 cm × 3.5 cm array. Packing ratio of wire arrays is 1/10 in speakers A, B and E due to a 30-$\mu$m distance between wires. Speaker C is doubly denser because the distance between wires is only 15 $\mu$m. According to anechoic room measurements, the sound pressure level in front of the loudspeakers behaves linearly in frequency range $2f_0 = 1 - 40$ kHz. An expression for exponentially growing pressure takes the form

$$P_{\mathrm{rms}} \approx y\bar{P}_J(2f_0)^p. \tag{18}$$

After fitting the data measured at 7 cm distance from speakers B and C into this expression, the resulting parameters were

$$p_B = 1.33 \pm 0.01 \ \& \ y_B = 0.38 \pm 0.05 \ \mu\mathrm{Pa}/(\mathrm{WHz})^p \tag{19}$$

$$p_C = 1.35 \pm 0.01 \ \& \ y_C = 0.19 \pm 0.03 \ \mu\mathrm{Pa}/(\mathrm{WHz})^p. \tag{20}$$

The same exponent was obtained in the case of speaker E ($p_E \approx 1.3$) while absolute SPL was somewhat higher ($y_E > y_B, y_C$). At lower frequencies than 1 kHz the frequency exponent was close to 1.5 in all loudspeakers.

The properties of an ideal thermoacoustic sound source were formulated as early as 100 years ago [1]. The heat capacity $C_s$ of the resistive loudspeaker must be minimized to reduce periodic heat loss induced by phase difference between Joule power and heat released by $C_s$. In VTT loudspeakers this has been implemented by reducing wire thickness into dozens of nanometers. Second, the heat flux from loudspeaker to air must be maximized via thermal decoupling. The air gap between wires and Si substrate is serving for that purpose in VTT loudspeakers. In recent years thermoacoustic research has focused mostly on homogenous thin films. Nanoscale layers of aluminium have been placed on top of porous silicon which acts as an efficient thermal insulator. Such devices show practically a flat spectrum in ultrasound range, but acoustic efficiency of the Al layer is limited by direct thermal contact to the substrate [10, 11, 12]. Xiao and colleagues approached the problem of heat capacity $C_s$ with carbon nanotube (CNT) thin films [2]. The films radiate sound into full-space with frequency response exponent $p = 0.7 - 0.8$. Thermal waves are permitted to propagate freely in air and, thanks to sub-$\mu$m thickness of CNT films, heat capacity is minimal. Kozlov and colleagues planted CNT forests on top of a silicon substrate [3]. Height of such forests affects significantly the frequency response: tall stacks of nanotubes behave like half-space versions of the films studied by Xiao *et al.* and show a frequency exponent $p = 0.6 - 0.7$. On the other hand, short 32-$\mu$m forests produce a higher exponent $p = 1.1 - 1.2$ which is claimed to be caused by pronounced periodic heat flux from nanotubes to substrate.

Many details of thermoacoustic emission of sound are understood with analytical tools. Information on metallic films on top of porous silicon can be found in Refs. [10, 13], for example. Typically in ultrasound range thermal waves are expected to attenuate completely within the porous silicon layer and internal losses of the metallic film are neglected. In the full-space treatment of Xiao *et al.*, periodically heated planar surfaces (carbon nanotube films) were studied: heat was supplied by means of a boundary condition. Their root mean square pressure formula, which will be introduced later in this work, agrees nicely with experimental carbon nanotube acoustics also in Ref. [3]. In special assignment [7] two thermoacoustic loudspeakers were studied numerically. First the sound pressure emitted by a periodically heated spherical shell was derived analytically. The response of the shell grows with frequency exponent $p = 1.0$ at low frequencies and experiences a cut-off in ultrasound range. Second, the theory derived by Xiao *et al.* was numerically tested in an axisymmetric half-space domain where a circular disk was heated periodically. At low frequencies the curves were in excellent

agreement producing a frequency exponent $p = 1.0$, but in ultrasound range simulated pressure saturated faster.

In conclusion, theoretical studies of thermoacoustics have been able to explain the behaviour of sound-emitting thin films which are either free-standing or in direct contact to a substrate. However, understanding the properties of sparse and suspended VTT loudspeakers has so far remained a challenge. In this work acoustical experiments with VTT loudspeakers were continued with extended 150 kHz bandwidth. In addition to on-axis far-field pressure measurements, some data was collected in near field and off the acoustic axis. Checking the linearity of loudspeaker operation as a function of input power was also necessary. Second, the effects of speaker suspension were studied with analytic Green's function methods. The third objective of this work was to develop a realistic simulation model which is able to reproduce the features caused by suspension and sparse packing of loudspeakers. After finding a proper model, the simulator could be used to search for optimal parameters which include loudspeaker geometry, for instance. Finite element method (FEM) was selected as the first simulation platform. Sound radiation from metal wires was also simulated with a periodic boundary finite differences (FD) solver. The solver computed the response of an infinite array in near field. Only a single source wire needed to be modelled, and the radiation pattern consisted of a plane wave which is known to transform into a spherical wave in far field.

# 4 Methods

## 4.1 Thermoacoustic Green's functions

When sinusoidal time-dependency of acoustic fields is understood, temperature is divided into two parts: stationary $T_s$ and oscillating $Te^{-2i\omega t}$. By assumption, pressure doesn't have any stationary component on top of ambient $P_0$, and the oscillating field is $Pe^{-2i\omega t}$. The PDEs are greatly simplified when time derivatives are replaced with $\partial_t = -2i\omega$: Diffusion equation (1) becomes

$$\nabla^2 T_s + \nabla^2 Te^{-2i\omega t} + \frac{2i\omega}{\alpha}Te^{-2i\omega t} + \frac{S}{\kappa} = \frac{2i\omega}{\kappa}Pe^{-2i\omega t} \tag{21}$$

and the time-harmonic expression of wave equation (2) is

$$\left(\nabla^2 P + \frac{4\omega^2}{c_T^2}P - \frac{4\omega^2 \rho_0}{T_0}T\right)e^{-2i\omega t} = 0. \tag{22}$$

This section describes an analytic framework for separating out the effect of sound source suspension which has crucial importance in VTT loudspeakers. Heat conduction along the sound-emitting wires, on the other hand, is basically negligible. Despite the nanoscale thickness of the wires, a macroscopic model of conduction (Fourier's law) is sufficient because the mean free path of electrons is only a few nanometers in aluminium [14]. It is a straightforward task to calculate that periodic heat flux into supporting Al crossbars is small compared to periodic heat flux into air. Figure 2 shows an illustration of array simulation geometry without supporting structures. In the limit of low frequency sound radiation is omnidirectional since sound wavelength $\lambda_0$ is much longer than speaker dimensions. It can be thought that sound radiation is excited by a point source in that situation. If a thermoacoustic speaker has been suspended above a heat-absorbing plane, undesired periodic heat flux into the plane is remarkable when thermal wavelength $\lambda_T$ is longer than the source-plane distance. Half-space Green's functions can provide an analytic solution for this thermoacoustic problem if the plane in question is extended into infinity. The geometry of this problem is drawn in Figure 3. The power density of an electrically unbiased point source of heat is

$$S = \bar{P}_J \left(1 + e^{-2i\omega t}\right)\delta(x)\delta(y)\delta(z - g) \tag{23}$$

of which only the oscillating part has acoustical significance. Air gap $g$ is the distance from source to $xy$-plane. Average AC power is of course $\bar{P}_J = V_{\text{ac}}^2/(2R)$. At the edge of half-space ($z = 0$) the boundary is taken to be acoustically hard ($\frac{\partial P}{\partial n} = 0$) but an impedance condition holds for temperature: $\frac{\partial T}{\partial n} - \gamma T = 0$. Three common thermal boundary conditions are
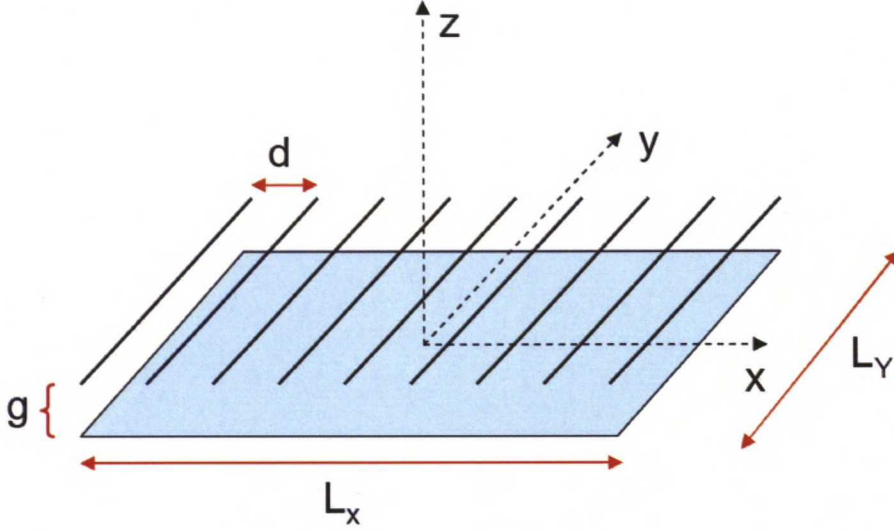
Figure 2: Three-dimensional illustration of a suspended array loudspeaker without supporting structures. Suspension parameter (air gap) is $g$ and distance between wires is $d$. Rectangular dimensions are $(L_x \times L_y)$.

1. Insulating boundary: $\gamma = 0$

2. Perfect heat sink as boundary: $T = 0$ $(\gamma \to \infty)$

3. Finite heat capacity per unit area: $\gamma = \frac{2i\omega C_{s,Si} - \beta_{0,Si}}{\kappa}$.

Here for convenience the boundary material is silicon with surface parameters $C_{s,Si}$ and $\beta_{0,Si}$. For all finite distances $g > 0$ the point source of sound operates without internal losses. This is a means of separating out the effect of source suspension. When taking the limit $g \to 0$, $C_{s,Si}$ and $\beta_{0,Si}$ become internal losses of the source and one should be able to retrieve the analytic results of Ref. [2] where sound was similarly emitted from a periodically heated plane. As the coupling $2i\omega P/\kappa$ is relatively weak in time-harmonic diffusion equation (21) it can be dropped out altogether:

$$(\nabla^2 + K)T \approx -\frac{\bar{P}_J}{\kappa}\delta(x)\delta(y)\delta(z - g) \tag{24}$$

where $K = 2i\omega/\alpha$ and $\sqrt{K} = \sqrt{\omega/\alpha}(1 + i) = k_T(1 + i)$. Essentially, the oscillating temperature field is a solution of a half-space Helmholtz problem in three dimensions.
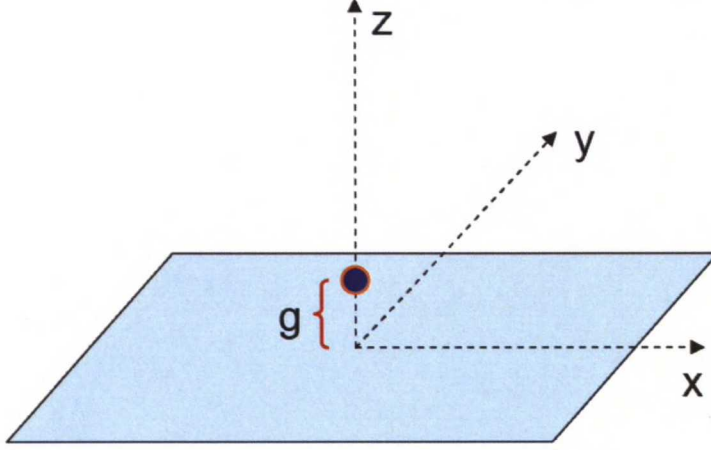
Figure 3: Three-dimensional radiation problem in half-space. A point source has been suspended at $z = g$ above an infinite substrate.

The free-space Green's function $G(\vec{r}_0, g) = G(\vec{r}_0 - g\hat{e}_z)$, which is the fundamental solution of 3D Helmholtz problem, is defined as

$$(\nabla^2 + K)G(\vec{r}_0, g) = -\delta(x)\delta(y)\delta(z - g) \;\Leftrightarrow\; G(\vec{r}_0, g) = \frac{e^{i\sqrt{K}|\vec{r}_0 - g\hat{e}_z|}}{4\pi|\vec{r}_0 - g\hat{e}_z|} \quad (25)$$

where $\vec{r}_0 = (x, y, z)$ and unit vector $\hat{e}_z$ is pointing in $z$-direction. In order to evaluate temperature $T(\vec{r}_0) = \bar{P}_J G_T(\vec{r}_0, g)/\kappa$ in half-space, the half-space Green's function $G_T$ must be made to fulfill the desired boundary condition. The correct forms of $G_T$ are readily found in literature [15, 16]:

1. Insulating $G_T = G(\vec{r}_0, g) + G(\vec{r}_0, -g)$

2. Sink $G_T = G(\vec{r}_0, g) - G(\vec{r}_0, -g)$

3. Finite impedance
   $G_T = G(\vec{r}_0, g) + G(\vec{r}_0, -g) + 2i\gamma \int_{-\infty}^{0} G(\vec{r}_0, -g + is)e^{-i\gamma s}ds.$

If the impedance $\gamma$ is an arbitrary complex number, the integral over $s$ converges but it is unfortunately not solvable in closed form. However, pressure field can be evaluated in far field $r_0 = |\vec{r}_0| \gg \lambda_T + g$ despite of this drawback. After re-organizing the time-harmonic wave equation with the help of isothermal wavenumber $k_P = 2\omega/c_T$, the 3D Helmholtz form is retrieved again:

$$(\nabla^2 + k_P^2)P = \frac{4\omega^2 \rho_0}{T_0}T. \quad (26)$$

11

The pressure field Green's function $G_P(\vec{r}_0, g)$ in half-space fulfills

$$(\nabla^2 + k_P^2)G_P = -\delta(x)\delta(y)\delta(z - g)$$

$$\Leftrightarrow G_P(\vec{r}_0, g) = \frac{e^{ik_P|\vec{r}_0 - g\hat{e}_z|}}{4\pi|\vec{r}_0 - g\hat{e}_z|} + \frac{e^{ik_P|\vec{r}_0 + g\hat{e}_z|}}{4\pi|\vec{r}_0 + g\hat{e}_z|} \tag{27}$$

where the hard boundary condition has been applied. In far field $G_P \approx \exp(ik_Pr_0)/2\pi r_0$ because the phase shift of reflected waves, which corresponds to a distance no longer than $2g$, is negligible. The pressure field is given by a troublesome convolution integral over half-space

$$\begin{aligned} P(\vec{r}_0) &= \frac{4\omega^2\rho_0}{T_0}\int_{z' \geq 0} G_P(\vec{r}_0 - \vec{r}')T(\vec{r}')d\vec{r}' \\ &= \frac{4\omega^2\rho_0\bar{P}_J}{\kappa T_0}\int_{z' \geq 0} G_P(\vec{r}_0 - \vec{r}')G_T(\vec{r}')d\vec{r}' \\ &\approx \frac{4\omega^2\rho_0\bar{P}_J}{\kappa T_0}G_P(\vec{r}_0)\int_{z' \geq 0} G_T(\vec{r}')d\vec{r}', \end{aligned} \tag{28}$$

where the last form is a far-field simplification: $G_P$ can be taken out of the integral because temperature has effectively decayed to zero there. The three-dimensional ($\vec{r}' = (x', y', z')$) convolution integral follows from Sommerfeld radiation condition

$$\lim_{r_0 \to \infty} r_0\left(\frac{\partial}{\partial r_0} - ik_P\right)P = 0 \tag{29}$$

which states that no energy radiates from infinity into the field [17]. Pressure is now linearly proportional to the spatial integral over $G_T$. When considering the fundamental Green's function associated to a source at $(0, 0, g)$, variables can be changed from $(x', y', z' - g)$ into spherical coordinates $(q, \theta, \varphi)$. $G(\vec{r}_0, g)$ becomes $G(q, \theta, \phi) = \exp(i\sqrt{K}q)/(4\pi q)$ where $q^2 = x'^2 + y'^2 + (z' - g)^2$. It's important to notice that fictitious temperature field in region $z' < 0$ doesn't act as pressure source. Therefore $\theta$ will only take values from 0 to $\pi/2 + \arcsin(g/q)$ when $q > g$, and the integral over half-space becomes

$$I_1 = \frac{1}{4\pi}\int_0^{2\pi} d\varphi \int_0^\infty \int_0^{\pi/2 + \arcsin(\min\{1, g/q\})} \frac{e^{i\sqrt{K}q}}{q}q^2 \sin\theta d\theta dq. \tag{30}$$

Separate treatment of $q > g$ and $q \leq g$ gives damped cosine and sine integrals

$$I_1 = \frac{1}{2}\left(\int_0^\infty qe^{i\sqrt{K}q}dq + \int_0^g qe^{i\sqrt{K}q}dq + g\int_g^\infty e^{i\sqrt{K}q}dq\right) \tag{31}$$

that can be solved using integration by parts and the result is

$$I_1 = \frac{i}{2k_T^2}\left(1 - \frac{e^{(i-1)k_Tg}}{2}\right). \tag{32}$$

12

A similar treatment to image source $G(\vec{r}_0, -g)$ gives

$$I_2 = \frac{ie^{(i-1)k_T g}}{4k_T^2} \tag{33}$$

and the complex pressure field in the case of insulating (sink) boundary condition is

$$P_{1,2}(\vec{r}_0) = \frac{2\omega^2 \rho_0 \bar{P}_J e^{ik_P r_0}}{\pi r_0 \kappa T_0} (I_1 \pm I_2). \tag{34}$$

The wavenumber is somewhat erroneous ($k_P > k_0$), but root mean squared pressure is not affected by this discrepancy. The rms value can be obtained by dividing pressure amplitude by $\sqrt{2}$. The insulating boundary condition provides actually an ultimate upper bound of thermoacoustically excited pressure:

$$P_{1,rms}(\vec{r}_0) = \frac{\bar{P}_J(2f_0)}{\sqrt{2}r_0 c_P T_0} \tag{35}$$

This formula is entirely free from loss mechanisms other than those fundamentally intrinsic to thermoacoustics. Theoretical sound radiation from a periodically heated spherical shell has the same form at low sound frequencies in special assignment [7]. On the other hand, the proximity to a heat sink detoriates the acoustic performance:

$$P_{2,rms}(\vec{r}_0) = \frac{\bar{P}_J(2f_0)}{\sqrt{2}r_0 c_P T_0} \sqrt{1 - 2e^{-k_T g}\cos(k_T g) + e^{-2k_T g}}. \tag{36}$$

In the limit of low frequency or, alternatively, small $g$ this formula can be linearized. That is to say, all contributions of the form $(k_T g)^3$ and higher vanish inside the square root. The linearization leads to a significant simplification which scales linearly with $g$:

$$P_{2,rms}(\vec{r}_0) \approx \sqrt{\frac{\pi}{\alpha}} \frac{\bar{P}_J g(2f_0)^{3/2}}{r_0 c_P T_0}. \tag{37}$$

When the boundary condition is of the third impedance type an integral $I_3$ must be solved:

$$I_3 = 2i\gamma \int_{-\infty}^{0} \frac{i}{4k_T^2} e^{(i-1)k_T(g-is)} e^{-i\gamma s} ds. \tag{38}$$

Spatial integration over $G(\vec{r}_0, -g+is)$ has already been done here; the result is $I_2$ in Eq. (33) equipped with transformation $g \mapsto g-is$. Complex pressure will be

$$P_3(\vec{r}_0) = \frac{2\omega^2 \rho_0 \bar{P}_J e^{ik_P r_0}}{\pi r_0 \kappa T_0} (I_1 + I_2 + I_3) \tag{39}$$

13

where the sum of the three integrals is

$$I_1 + I_2 + I_3 = \frac{1}{2k_T^2} \left( i - \frac{\gamma e^{(i-1)k_T g}}{k_T + i(k_T - \gamma)} \right). \tag{40}$$

Pressure $P_3$ can be easily root mean squared in the limit of small $\beta_{0,Si}$ using $\gamma = i\delta = i2\omega C_{s,Si}/\kappa$. At this point it would be worth noting that $C_{s,Si}/\kappa$ is actually frequency-dependent because thermal waves attenuate rapidly in bulk materials, too. Hence, only a thin surface slab will contribute to the impedance, and the thickness of the slab can be presented in terms of skin depth, the depth where ratio of wave amplitude to its surface value is $1/n$. The skin depth is of the form

$$z_n = \sqrt{\frac{\alpha_{Si}}{\omega}} \ln n \tag{41}$$

where $\alpha_{Si}$ is diffusion constant of silicon [18]. A proper value for heat capacity per unit area would be

$$C_{s,Si} = C_{Si} z_n \tag{42}$$

where $C_{Si}$ is bulk heat capacity per unit volume of silicon. In Eq. (41) it is possible to choose $\ln n = 1$. The estimate for rms pressure is

$$P_{3,rms}(\vec{r}_0) = \frac{\bar{P}_J(2f_0)}{\sqrt{2} r_0 c_P T_0} \cdot \frac{|k_T + \delta + ik_T - \delta e^{(1-i)k_T g}|}{\sqrt{k_T^2 + (k_T + \delta)^2}}. \tag{43}$$

Imaginary part of impedance $\delta$ can be expressed like

$$\delta = \frac{2C_{Si}\sqrt{\pi(2f_0)\alpha_{Si}}}{\kappa} \tag{44}$$

and plugged into the final form

$$P_{3,rms}(\vec{r}_0) = \frac{\bar{P}_J(2f_0)}{\sqrt{2} r_0 c_P T_0}$$
$$\times \sqrt{1 - \delta e^{-k_T g} \cdot \frac{2k_T \sin(k_T g) + 2(k_T + \delta)\cos(k_T g) - \delta e^{-k_T g}}{k_T^2 + (k_T + \delta)^2}}. \tag{45}$$

In the limit $\frac{\delta}{k_T} \gg 1$, i.e., when the heat capacity is large, this formula approaches the heat sink equation (36). In the opposite limit where $(k_T g)$ is large or $\frac{\delta}{k_T} \ll 1$ the formula begins to look exactly like the ultimate pressure in equation (35). When plotting $P_{3,rms}$ on a logarithmic scale as a function

of frequency, the gradient (instantaneous frequency exponent) resides in the range $1.0 - 1.5$. Linearization of Eq. (45) with respect to $(k_T g)$ gives

$$P_{3,rms}(\vec{r}_0) \approx \frac{\bar{P}_J(2f_0)}{\sqrt{2}r_0 c_P T_0} \cdot \sqrt{1 - \delta \cdot \frac{2k_T(1 - k_T^2 g^2) + \delta(1 - 2k_T^2 g^2)}{k_T^2 + (k_T + \delta)^2}}, \quad (46)$$

which does not actually provide additional insight. Using the exact form of Eq. (45) would be preferable. In the limit of low frequency, loudspeaker heat capacity has no acoustical contribution and the thermophysical substrate effect is alone responsible for weakened acoustic performance. It can be expected that equation (45) is able to explain sound radiation from VTT loudspeakers in audible range of frequencies. This is enabled also by the fact that speaker array sparsity has only a little effect there. In ultrasound range, however, radiated sound pressure levels are likely to be overestimated because speaker heat capacity is neglected.

## 4.2 Planar homogenous loudspeakers

In Ref. [2] Xiao and colleagues derived the formula of sound radiation from a two-sided thin film. Film area was assumed to be so large ($\sqrt{A} \gg \lambda_T$) that emitted thermal waves could be treated with one-dimensional diffusion equation

$$\alpha \partial_z^2 T + 2i\omega T = 0. \quad (47)$$

Pressure coupling $2i\omega P/\kappa$ was neglected and the solution was a linear combination of waves $e^{\sigma z}$ and $e^{-\sigma z}$ with exponent $\sigma = k_T(i - 1)$. Placing the loudspeaker in the origin made regions $z < 0$, $z > 0$ symmetric and the Joule power boundary condition could be written as

$$\bar{P}_J = -2i\omega A C_s T(0) - 2A\kappa\partial_z T(0^+) + 2A\beta_0 T(0) \quad (48)$$

where $z = 0^+$ denotes the front interface. The heat capacity was shared by the two surfaces. In region $z \geq 0$ the thermal wave is as simple as $T(z) = B_3 e^{\sigma z}$ which decays to zero at infinity. Prefactor $B_3$ is obtained now from boundary condition

$$\bar{P}_J = -2AB_3(i\omega C_s + \kappa\sigma - \beta_0). \quad (49)$$

An imaginary thermoacoustic piston can be constructed from the two air slabs ($\lambda_T \times A$) where thermal waves are present. This was done in Ref. [2] but it is also possible to utilize the fundamental Green's function of 3D Helmholtz problem. Assuming that sound radiation is omnidirectional ($\sqrt{A} \ll \lambda_0$), it

is possible to revisit convolution in Eq. (28). Full-space Green's function $G_P = \exp(ik_P r_0)/(4\pi r_0)$ is used this time:

$$P(r_0) = \frac{4\omega^2 \rho_0}{T_0} \cdot \frac{e^{ik_P r_0}}{4\pi r_0} \int_{\mathbb{R}^3} T(\vec{r}')d\vec{r}'. \tag{50}$$

This formula can always be utilized in the limit of omnidirectional sound radiation; the temperature profile in the integral can be arbitrary. In the thin-film simplification the integral reduces to $2A\int_0^\infty B_3 e^{\sigma z'} dz' = -2AB_3/\sigma$. Root mean squared pressure takes the value

$$P_{\text{rms}}(r_0) = \frac{\omega^2 \rho_0 \bar{P}_J}{\sqrt{2}r_0 T_0 |\sigma(i\omega C_s + \kappa\sigma - \beta_0)|} \tag{51}$$

which can be processed further:

$$P_{\text{rms}}(r_0) = \frac{\bar{P}_J(2f_0)}{2\sqrt{2}c_P r_0 T_0} \cdot \sqrt{\frac{2(2f_0)}{(\sqrt{(2f_0)} + \sqrt{f_1})^2 + \left(\sqrt{(2f_0)} + \frac{(2f_0)\sqrt{f_1}}{f_2}\right)^2}}. \tag{52}$$

Constant frequencies are defined as $f_1 = \alpha\beta_0^2/(\pi\kappa^2)$ and $f_2 = \beta_0/(\pi C_s)$. The half-space equivalent of this formula can be found by letting $g$ approach zero in Eqs. (39) & (40). Only one side of the thin film will radiate sound in that case. Full-space prefactor $1/2$ will vanish and $f_2$ must be re-defined: $f_2 = \beta_0/(2\pi C_{s,Si})$. Of course, the Green's function formalism is also compatible with Arnold and Crandall's theory of thermoacoustic thin films. Vanishing suspension ($g \to 0$) and substantial heat capacity ($\delta \gg k_T$) in Eq. (43) nicely reveal

$$P_{\text{rms}} \approx \frac{\bar{P}_J(2f_0)k_T}{r_0 c_P T_0 \delta} \propto \frac{\sqrt{2f_0}}{C_{s,Si}}. \tag{53}$$

Eqs. (51) and (52) describe the free-standing case. The associated phase difference between Joule power and surface temperature is (see Ref. [2])

$$\bar{\phi} = \arg B_3 = \arctan\left(\frac{\omega C_s + \kappa k_T}{\beta_0 + \kappa k_T}\right) \tag{54}$$

which is small at low frequencies and approaches $\pi/2$ in the limit of high frequency. However, in the ultimate limit where $C_s$ and $\beta_0$ approach zero the phase difference is a constant $\bar{\phi} = \pi/4$. It would be interesting to see if $\bar{\phi}$ changes when the thin film is placed near an impedance plane. A heat-absorbing impedance plane will at least lower the surface temperature of the film. In front of the film ($z \geq g$) thermal waves take again the form $T(z) = B_3 e^{\sigma z}$ but behind the film ($0 \leq z \leq g$) a reflected wave is also present: $T(z) = B_1 e^{\sigma z} + B_2 e^{-\sigma z}$. Heat flux is obviously discontinuous on the interface of these regions:

$$\bar{P}_J = -2i\omega AC_s T(g) + A\kappa(\partial_z T(g^-) - \partial_z T(g^+)) \tag{55}$$

16

where $\beta_0$ is dropped out altogether. The ratio of $B_1$ to $B_2$ can be found using the impedance boundary condition from previous section of this work:

$$\kappa \partial_z T(0) + 2i\omega C_{s,Si} T(0) = 0. \tag{56}$$

This gives

$$b = \frac{B_1}{B_2} = \frac{\kappa\sigma - 2i\omega C_{s,Si}}{\kappa\sigma + 2i\omega C_{s,Si}}. \tag{57}$$

Of course, temperature $T(g)$ at the surface is continuous and $B_3$ can thus be expressed in terms of $B_2$:

$$B_3 = B_2(b + e^{-2\sigma g}). \tag{58}$$

Consequently, Eq. (55) turns into

$$\bar{P}_J = -2AB_2(i\omega C_s(be^{\sigma g} + e^{-\sigma g}) + \kappa\sigma e^{-\sigma g}) \tag{59}$$

and the phase of surface temperature is

$$\bar{\phi} = \arg T(g) = \arg\left(-\frac{b + e^{-2\sigma g}}{i\omega C_s(be^{\sigma g} + e^{-\sigma g}) + \kappa\sigma e^{-\sigma g}}\right). \tag{60}$$

Pressure field can again be calculated with convolution formula Eq. (28) and the half-space Green's function $G_P = \exp(ik_P r_0)/(2\pi r_0)$. In this treatment pressure waves are able to penetrate the thin film and their root mean square value is

$$P_{\text{rms}}(r_0) = \frac{\sqrt{2}\omega^2 \rho_0}{\pi r_0 T_0}\left|\frac{-AB_2(2e^{-\sigma g} + b - 1)}{\sigma}\right|. \tag{61}$$

With the aid of Eq. (59) the formula becomes

$$P_{\text{rms}}(r_0) = \frac{\bar{P}_J f}{\sqrt{2}c_P r_0 T_0}\left|\frac{e^{-\sigma g} + \frac{b-1}{2}}{\frac{i\omega C_s}{\kappa\sigma}(be^{\sigma g} + e^{-\sigma g}) + e^{-\sigma g}}\right|. \tag{62}$$

It can be expected that this equation fails to explain sound radiation from sparse loudspeakers when thermal wavelength is as short as the loudspeaker inner dimensions.

## 4.3 Computational methods

### 4.3.1 Circular wires

According to equations (15) and (16) circular loudspeakers produce the same on-axis ($\theta = 0$) frequency response as rectangular loudspeakers if their surface areas are equal. A thermoacoustic simulation platform can thus be defined in cylinder coordinate system. Taking advantage of axisymmetry helps to eliminate one spatial coordinate $\varphi$. Finite element method in near field can be utilized in a triangular mesh covering a quarter of a circle in $rz$-plane. This idea has been successfully tested in the case of homogenous disk loudspeaker in special assignment [7]. Simulating equidistant wires in an axisymmetric system would be possible if the wires were circular. A 0.5 cm$^2$ circular array would comprise about 130 wires when the spacing $d$ is 30 $\mu$m. However, trying to place more than a hundred cross-sections on $rz$-plane and then creating a hyperfine mesh around them would lead to undesired computational complexity. Fortunately, the cross-section of wires in VTT loudspeakers is so tiny that its dimensions are much shorter than wavelengths of sound and temperature if frequency $2f_0$ doesn't exceed 1 MHz. Finite element method is capable of solving PDEs that have delta distributions as sources: why not consider periodic heat supply in the form of delta functions $\delta$? A sketch of a suspended array of circular wires in cylinder coordinate system can be found in Figure 4.

In diffusion equation (1) the integral of arbitrary source $S$ over half-space must give net heat supply per unit time. In the array model $S$ is a sum of wire-specific delta functions. To take the air gap into account, the $z$-coordinate of wires can be fixed to $z = g$. The $r$-coordinates $r_k$ can be deduced from two rules: Because of symmetry the first wire is located at ($r_1 = \frac{d}{2}, g$). To keep the distance between wires constant, $r_k - r_{k-1} = d$ for all $k \in \{2, 3, ..., N_w\}$.

The distribution function of a single wire in $S$ is easily found to be

$$\psi(r, z; g, k) = \frac{\delta(r - r_k)\delta(z - g)}{2\pi r_k} \tag{63}$$

and net heat supply per unit time consists of electric power minus losses related to $C_s$ and $\beta_0$. Hence, the expression for $S$ is (compare with equation
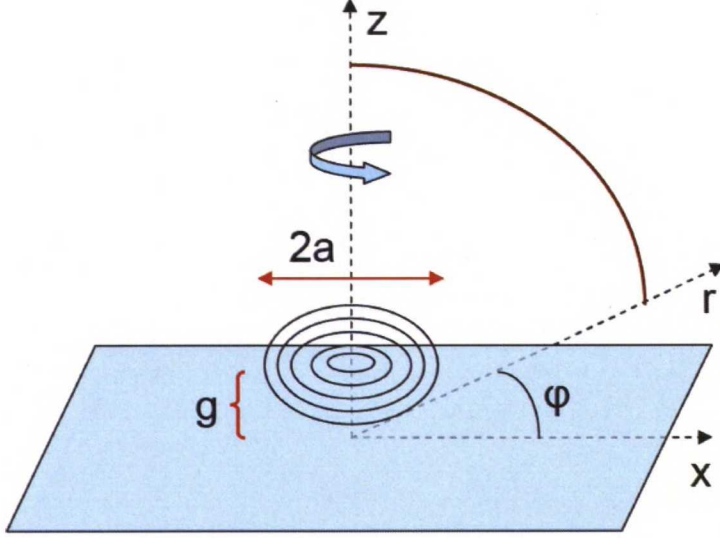
18

Figure 4: Three-dimensional radiation problem in half-space ($r, \varphi, z \geq 0$). An axisymmetric array of wires has been suspended at $z = g$ above an infinite substrate. Array radius is $a$. The brown arc will draw the spherical near-field domain while rotating around $z$-axis.

(6))

$$S = \sum_{k=1}^{N_w} \left( P_{J,k} - A_k \beta_0 T - A_k C_s \dot{T} \right) \psi(r, z; g, k). \tag{64}$$

Wire-specific areas $A_k$ and electric powers $P_{J,k}$ must grow linearly with radial coordinate $r_k$. Otherwise the heat supply wouldn't be homogenous in the array.

$$P_{J,k} = \begin{cases} P_J \frac{r_k^2 - r_{k-1}^2}{a^2} & 2 \leq k \leq N_w \\ P_J \frac{r_1^2}{a^2} & k = 1 \end{cases} \tag{65}$$

$$A_k = \pi w(w + 2r_k), \tag{66}$$

where $w = 3$ $\mu$m is the constant width of wires.

Next the computational domains and boundaries must be designed to adapt to the array radius $a = r_{Nw}$. At sound frequencies below 1 MHz thermal wavelength $\lambda_T$ is always shorter than sound wavelength $\lambda_0$. The axisymmetric triangular mesh in $rz$-plane should fulfill several conditions:

1. Near field is enclosed by the spherical domain
   $\Omega = \{(r, z) \in \mathbb{R}^2 \mid r \geq 0, z \geq 0 \ \& \ b^2 \leq r^2 + z^2\}$

19

2. Distance between nodes doesn't exceed $\lambda_0/16$. However, on the boundaries a refinement $\lambda_0/64$ is necessary

3. Thermal waves are taken into account by selecting a spacing parameter $\lambda_T/32$ when the distance from wires $(r_k, g)$ is smaller than $\lambda_T$.

The overall domain can be expanded beyond near field when necessary. Spherical radius $b$ can be increased in order to probe into far field with the triangular mesh. Alternatively, all half-space can be discretized with infinite elements to obtain unbounded solutions. After dividing the boundary $\partial\Omega = \Gamma$ into subsections, boundary conditions must be introduced for fields $P$ and $T$ and their time derivatives $Y = \dot{P}$ and $X = \dot{T}$. The purpose of $X$ and $Y$ is to avoid second-order derivatives with respect to time.

- $\Gamma_1 = \{(r, z) \in \mathbb{R}^2 \mid r = 0\}$:
  Axisymmetry: $\frac{\partial P}{\partial n} = \frac{\partial Y}{\partial n} = \frac{\partial X}{\partial n} = 0$

- $\Gamma_2 = \{(r, z) \in \mathbb{R}^2 \mid r \geq 0, z \geq 0 \,\&\, b^2 = r^2 + z^2\}$:
  Absorbing boundary for bounded problem: $\frac{\partial P}{\partial n} = -\frac{Y}{c_0} - \frac{P}{b}$ [19]
  Thermal waves have decayed to zero: $X = 0$

- $\Gamma_3 = \{(r, z) \in R^2 \mid 0 \leq r \leq b \,\&\, z = 0\}$:
  Rigid substrate behind wires has large heat capacity $C_{s,Si}$:
  $\frac{\partial P}{\partial n} = \frac{\partial Y}{\partial n} = 0$ and $\frac{\partial X}{\partial n} = -\frac{C_{s,Si}}{\kappa}\dot{X}$

- In the unbounded problem $P$ and $\nabla P$ must vanish at infinity according to Sommerfeld radiation condition [17].

### 4.3.2 Anechoic time-discretized problem

The performance of absorbing boundary condition is always limited by quality of discretization. Especially when the wave vector of sound is not perpendicular to the boundary, some reflection will unavoidably take place. If the sampling of pressure is performed on $z$-axis at distance $z_s < b$ from the wires, when does the first echo return to the sampling point? The answer is $(b - z_s)/c_0$ seconds after pressure waves have hit the boundary $\Gamma_2$ for the first time. The finite speed of sound is exploited in the following method: it does not matter whether the absorbing boundary is functional as long as the reflections don't influence the results. This can be called the quasi-anechoic way of simulating sound radiation in free field.

A time-discretized solution with zero initial condition can be obtained with finite element method. Joule power is switched on all of a sudden: it is

20

possible to check how pulsed input signals are reproduced thermoacoustically. PDE (2) can be expressed in the form

$$\frac{1}{c_T^2}\dot{Y} - \frac{\rho_0}{T_0}\dot{X} = \Delta P. \tag{67}$$

Multiplying it with test function $w \in W = H^1(\Omega)$ and integrating over $\Omega$ gives

$$\int_\Omega w\left(\frac{\dot{Y}}{c_T^2} - \frac{\rho_0\dot{X}}{T_0}\right)d\vec{r} = -\int_\Omega \nabla w \cdot \nabla P d\vec{r} - \int_{\Gamma 2} w\left(\frac{Y}{c_0} + \frac{P}{b}\right)dS \tag{68}$$

where Green's first theorem has been applied. The integrals over domain $\Omega$ are two-dimensional and path integrals take care of the boundaries $\Gamma_n$. Eliminating $Y$ would simplify the other PDE that has to be solved: a combination of PDEs (1) and (2) looks like

$$\dot{X} = \frac{\alpha c_0^2}{\kappa}\Delta P + \frac{\alpha c_0^2}{c_T^2}\left(\Delta X + \frac{\dot{S}}{\kappa}\right). \tag{69}$$

The corresponding test function will have to agree with the Dirichlet boundary condition described above: $v \in V = \{v \in H^1(\Omega) \mid v = 0, (r, z) \in \Gamma_2\}$. After following the same procedure as above,

$$\int_\Omega v\dot{X}d\vec{r} + \frac{\alpha c_0^2}{\kappa} - \int_\Omega \nabla v \cdot \nabla P d\vec{r}$$
$$= -\frac{\alpha c_0^2}{c_T^2}\left(\int_\Omega\left(\nabla v \cdot \nabla X - \frac{v\dot{S}}{\kappa}\right)d\vec{r} + \frac{C_{s,Si}}{\kappa}\int_{\Gamma 3} v\dot{X}dS\right). \tag{70}$$

The thermoacoustic solution can be found by searching for fields $X$, $Y$ and $P$ that satisfy equation (68) for every $w \in W$ and equation (70) for every $v \in V$.

An easy starting point would be to follow Ritz-Galerkin procedure for piecewise linear finite elements [20]. For each node $\vec{r}_i$ in the mesh there's a linear shape function $\varphi_i(\vec{r})$ which satisfies $\varphi_i(\vec{r}_j) = \delta_{ij} \, \forall i, j$. Of course, $\delta_{ij}$ is the Kronecker delta. Physical quantities can be expressed using the shape functions as a basis: for example, $P = \sum_i \xi_{P,i}\varphi_i$. The scalar coefficients $\xi_{P,i}$ are the degrees of freedom that are eventually solved. They can be collected together into column vectors ($\xi_P$ contains nodal values of pressure, for example) of length $N$ which is the number of nodes. Replacing $v$ and $w$ with $\varphi_j$ leads the problem into linear equation systems: Eq. (68) becomes

$$\frac{M\dot{\xi}_Y}{c_T^2} - \frac{\rho_0 M\dot{\xi}_X}{T_0} = -\hat{S}\xi_P - M_2\left(\frac{\xi_Y}{c_0} + \frac{\xi_P}{b}\right) \tag{71}$$

where one can identify some common matrices that appear in finite element method:

- Mass matrix $(M)_{ij} = \int_\Omega \varphi_i \varphi_j d\vec{r}$, $d\vec{r} = 2\pi r dr dz$

- Mass matrix on boundary $\Gamma_n$ $(M_n)_{ij} = \int_{\Gamma n} \varphi_i \varphi_j dS$

- Stiffness matrix $(\hat{S})_{ij} = \int_\Omega \nabla \varphi_i \cdot \nabla \varphi_j d\vec{r}$.

The size of these symmetric matrices is determined by the number of nodes in the mesh: it is $N \times N$. The constant prefactor $2\pi$ that results from integrating over the polar angle of the coordinate system will be dropped out of the matrices. Equation (70) becomes

$$M\dot{\xi}_X + \frac{\alpha c_0^2}{\kappa}\hat{S}\xi_P + \frac{\alpha c_0^2}{c_T^2}\left(\hat{S}\xi_X + \frac{C_{s,Si}}{\kappa}M_3\dot{\xi}_X\right)$$
$$= \frac{\alpha c_0^2}{2\pi\kappa c_T^2}\left(\dot{P}_J b_w - \beta_0 M_w \xi_X - C_s M_w \dot{\xi}_X\right) \tag{72}$$

in which time derivative of total electric power is $\dot{P}_J = 2\pi f_0 V_{ac}^2 \sin(4\pi f_0 t)/R$. There are also wire-specific structures where $k$ is wire index running from 1 to $N_w$:

- A special wire matrix $(M_w)_{ij} = \sum_k A_k \varphi_i(\vec{r}_k)\varphi_j(\vec{r}_k)$

- and a special wire vector $(b_w)_i = \sum_k \frac{r_k^2 - r_{k-1}^2}{a^2}\varphi_i(\vec{r}_k)$.

A reliable way of doing time discretization is implicit Crank-Nicholson method [18]. Time is divided into constant intervals $t^n = n\Delta t$. Time derivatives are calculated in the middle of two consequent steps:

$$\dot{\xi}_T^{n+1/2} \approx \frac{\xi_T^{n+1} - \xi_T^n}{\Delta t}. \tag{73}$$

This example can reveal the logic behind the Crank-Nicholson scheme:

$$\dot{\xi}_T^{n+1/2} = \xi_X^{n+1/2} \Leftrightarrow \xi_T^{n+1} = \xi_T^n + \frac{\Delta t}{2}(\xi_X^{n+1} + \xi_X^n) \tag{74}$$

which explains time evolution of temperature; for pressure holds $\xi_P^{n+1} = \xi_P^n + \frac{\Delta t}{2}(\xi_Y^{n+1} + \xi_Y^n)$.

The two semidiscretized linear equation systems (71) and (72) can be fully discretized and then combined into a single system of size $2N$ where Dirichlet boundary condition has been activated on $\Gamma_2$ boundary nodes. In computations one matrix inversion per time step is required. The maximum length of interval $\Delta t$ is limited by the stability of the problem. A more detailed overview of time discretization is presented in Appendix 2.

### 4.3.3 Unbounded time-harmonic problem

Previously it was noted that bounding of wave problems is a challenging task. A time-harmonic solver is particularly vulnerable to boundary conditions. A truncated computational domain can, however, be easily enlarged to cover all half-space. In single-frequency case this is enabled by infinite elements that are equipped with shape functions which have *a priori* information on the wave vector [21].

Transition from triangular near-field mesh into the infinite domain takes place on artificial boundary $\Gamma_2$. The absorbing boundary condition must of course be forgotten. Oscillating $P$ is calculated in the nodes of quadrilateral infinite elements. One edge of such an element is shared with a triangle and the opposite edge is located at infinity. The length of solution vector $\xi_P$ is increased by an integer $N_r$, the number of nodes in the infinite domain that do not intersect with boundary $\Gamma_2$. For the sake of convenience, infinite domain contributions to stiffness and mass matrices are denoted with $\hat{S}_r$ and $M_r$, respectively. The matrices are taken to be zero padded to full size $(N + N_r) \times (N + N_r)$.

Separation with respect to Fourier components is possible: the stationary part of equation (21) is

$$\nabla^2 T_s + \frac{1}{\kappa} \sum_k \left( \frac{V_{\mathrm{ac}}^2 (r_k^2 - r_{k-1}^2)}{2Ra^2} - A_k \beta_0 T_s \right) \psi(r, z; g, k) = 0 \qquad (75)$$

and the oscillating part looks like

$$\frac{2i\omega}{\kappa} P = \nabla^2 T + \frac{2i\omega}{\alpha} T$$
$$+ \frac{1}{\kappa} \sum_k \left( \frac{V_{\mathrm{ac}}^2 (r_k^2 - r_{k-1}^2)}{2Ra^2} - A_k \beta_0 T + 2i\omega A_k C_s T \right) \psi(r, z; g, k). \qquad (76)$$

Wire distribution function $\psi$ is in equation (63). The Ritz-Galerkin procedure of FEM gives two linear systems for the oscillating fields: in domain $\Omega$ diffusion equation is reduced to

$$-\hat{S}\xi_T + \frac{2i\omega C_{s,Si}}{\kappa} M_3 \xi_T + \frac{2i\omega}{\alpha} M\xi_T - \frac{2i\omega}{\kappa} M\xi_P$$
$$+ \frac{V_{\mathrm{ac}}^2}{4\pi \kappa R} b_w + \frac{2i\omega C_s - \beta_0}{2\pi\kappa} M_w \xi_T = 0 \qquad (77)$$

and the information on isothermal wave equation is present in

$$-\hat{S}\xi_P + \frac{4\omega^2}{c_T^2} M\xi_P = \frac{4\omega^2 \rho_0}{T_0} M\xi_T. \qquad (78)$$

23

Within the infinite elements, however, only the isentropic mode of acoustics is considered:

$$-\hat{S}_r \xi_P + \frac{4\omega^2}{c_0^2} M_r \xi_P = 0 \tag{79}$$

where mass and stiffness matrices have gained contributions from integrals over weighted shape functions. There will be an extra phase involved that makes the shape functions differ from simple polynomials $P_i$ that appear in the near-field domain $\Omega$:

$$\varphi_i(r,z) = P_i(r,z)e^{-ik_0\mu(r,z)} \tag{80}$$

Function $\mu$ represents the path propagated by the waves in the infinite domain. Obviously $\mu$ is zero on the boundary $\Gamma_2$ and everywhere in $\Omega$. In mass and stiffness integrals the new shape functions $\varphi_i$ are complex conjugated and given an additional weight $D(r,z)$. Function $D$ takes the value of unity on $\Gamma_2$ and in the infinite domain it is proportional to $1/b^2$ where $b = \sqrt{r^2 + z^2}$ is the radius in spherical coordinate system. Complex conjugation simplifies the integrals by removing the phase factors, and without $D$ the Sommerfeld radiation condition wouldn't be satisfied at infinity.

Solving the oscillating fields everywhere in half-space demands only one matrix inversion:

$$\begin{pmatrix} -\hat{S} + \frac{2i\omega C_{s,Si}}{\kappa} M_3 + \frac{2i\omega}{\alpha} M + \frac{2i\omega C_s - \beta_0}{2\pi\kappa} M_w & \left( -\frac{2i\omega}{\kappa} M \quad 0 \right) \\ \begin{pmatrix} -\frac{4\omega^2 \rho_0}{T_0} M \\ 0 \end{pmatrix} & -\hat{S}_r + \frac{4\omega^2}{c_0^2} M_r + \begin{pmatrix} -\hat{S} + \frac{4\omega^2}{c_T^2} M & 0 \\ 0 & 0 \end{pmatrix} \end{pmatrix}$$

$$\text{times} \begin{pmatrix} \xi_T \\ \xi_P \end{pmatrix} \text{ equals } -\frac{V_{\text{ac}}^2}{4\pi\kappa R} \begin{pmatrix} b_w \\ 0 \end{pmatrix}. \tag{81}$$

In Appendix 3 the definitions of matrices $\hat{S}_r$ and $M_r$ are summarized. Pressure and temperature vectors are complex-valued: modulus and argument are the amplitude of oscillation and phase difference between the field and electric power, respectively. It's good to remember that the vectors contain all the necessary information to probe into the field everywhere in half-space: this can be accomplished via interpolation of nodal values. Amplitude of oscillation and phase difference of the temperature on air-wire interfaces can thus be averaged: the respective symbols are $\bar{T}_w$ and $\bar{\phi}_w$. An estimate for the amplitude of thermal power that flows periodically through the air-wire interface is

$$P_{\text{air}} = \left| \frac{V_{\text{ac}}^2}{2R} - A\beta_0 \bar{T}_w e^{i\bar{\phi}_w} - 2\omega A C_s \bar{T}_w e^{i(\bar{\phi}_w - \pi/2)} \right| \tag{82}$$

where $A = \sum_k A_k$ equals $\pi a^2$ multiplied by the packing ratio of the array $w/d$. Time average of this heat flow is of course zero. Thermoacoustic efficiency describes how strongly oscillating pressure is coupled to $P_{\text{air}}$. Linear

24

theory of acoustics violates the law of conservation of energy because time average of acoustic power will turn out to be positive. Loudspeaker efficiency can thus irrationally exceed 100 % because acoustic power will be proportional to the square of electric power. However, current non-viscous theory will break down when the GHz range of frequencies is reached [6]. In conclusion, the simulations should be run at moderate electric input power and low enough ($2f_0 \leq 10^9$ Hz) frequency. Losses caused by radiation ($\beta_0$) are maximized when there phase difference $\bar{\phi}_w$ is zero: according to Eq. (54) this occurs when the frequency is infinitesimally low. On the other hand, $\bar{\phi}_w$ will approach $\pi/2$ in the limit of high frequency. Heat capacity $C_s$ lags more and more behind electric power when frequency is increased. The related loss is strengthened not only by prefactor $\omega$ but also by $\exp(i\bar{\phi}_w - i\pi/2)$ approaching unity which means that heat released by $C_s$ will be exactly in opposite phase compared to Joule input power.

Next, to find out thermoacoustic efficiency acoustic power radiated by the array must be estimated. Local acoustical intensity $I_{av}$ is proportional to the square of pressure when spherical wave assumption holds (see equation (13)). In order to fix a distance from far field, a circular arc in $rz$-plane is discretized. The arc has radius $b = \sqrt{r_i^2 + z_i^2}$ where spatial index runs from 1 to $N_\theta$ and $r_1 = z_{N\theta} = b$. The corresponding angles between $z$-axis and position vector $(r_i, z_i)$ are $\theta_i = \arctan(r_i/z_i)$ where $\Delta\theta = \theta_i - \theta_{i-1}$ is assumed to be constant. For each $i$ there is a corresponding surface area $S_i$ which is created when the arc rotates around $z$-axis. The sum of the areas must equal $2\pi b^2$, the area of halved spherical shell with radius $b$:

$$S_i = 2\pi b^2 \cdot \begin{cases} 1 - \cos(\frac{\Delta\theta}{2}) & i = 1 \\ 2\sin(\theta_i)\sin(\frac{\Delta\theta}{2}) & 1 < i < N_\theta \\ \sin(\frac{\Delta\theta}{2}) & i = N_\theta. \end{cases} \tag{83}$$

The integral in the definition of acoustic power (equation (14)), is transformed into sum

$$P_{\text{ac}} \approx \frac{1}{2\rho_0 c_0} \sum_i S_i |P(r_i, z_i)|^2 \tag{84}$$

which is plugged into the definition of thermoacoustic efficiency, the ratio of acoustic power amplitude to thermal power amplitude in air:

$$\eta_t = \frac{2P_{\text{ac}}}{P_{\text{air}}}. \tag{85}$$

The result from equation (82) is also inserted here, and prefactor 2 cancels out time averaging present in $P_{\text{ac}}$. The performance of the loudspeaker is fundamentally characterized by the ratio of acoustic output power to electric input power: $\eta = P_{\text{ac}}/\bar{P}_J$. The square root of this value is somewhat misleadingly called thermoacoustic coupling factor. At least in Ref. [10] the

quality of thermoacoustic loudspeakers is presented in terms of the coupling factor $\sqrt{\eta}$ at a fixed input power density $\bar{P}_J/A = 1$ W/cm$^2$. In linear regime of thermoacoustics $\eta_t$ and $\eta$ scale linearly with input power $\bar{P}_J$, and $\sqrt{\eta}$ is proportional to the square root of $\bar{P}_J$.

### 4.3.4  Infinite array approximation

Sound radiation from a macroscopic planar source can be understood as a wave conversion process. In near field, loudspeaker subdomains work in phase and generate a plane wave. At Rayleigh distance $R_0$ the plane wave is disrupted by interference effects which result from finite loudspeaker size. That is precisely when the plane wave begins to transform into a spherical wave. Interestingly, the pressure on the face of the loudspeaker (denoted with symbol $P_w$) can be uniquely restored from an on-axis pressure measurement in far field [8]:

$$P_{\text{rms}}(r_0) = \frac{P_w R_0}{\sqrt{2}r_0}. \tag{86}$$

This formula holds when $r_0$ is larger than $R_0$. The Rayleigh distance of a symmetric loudspeaker is given by

$$R_0 = \frac{A}{\lambda_0} \tag{87}$$

where surface $A$ needn't be circular. Remembering the fact that VTT loudspeakers are periodic wire arrays, it is possible to design a simulation platform with periodic boundary conditions. This of course neglects effects that emerge on speaker boundaries. In principle, the infinite array approximation corresponds to frequency range $\lambda_0, \lambda_T \ll a$. Thanks to periodicity, there is no need to simulate multiple wires, but array sparsity must be correctly implemented. Throughout this chapter the infinitely long wires are aligned in $y$-direction, wire separation is given in $x$-coordinates, and plane waves of sound propagate in $z$-direction (see Figure 2). Thermoacoustic PDEs can be solved with finite differences (FD) method in two-dimensional $xz$-domain that has dimensions ($d \times \lambda_0$). Due to domain periodicity, the single wire can be given arbitrary $x$-coordinates. The wire is assumed to be infinitesimally thin and discontinuity of heat flux on wire surface must be taken into account. Both full- and half-space simulators can be defined:

(a) Free-standing loudspeaker is located at the origin and plane waves are absorbed on two boundaries $z = \pm\lambda_0/2$. Full-space pressure can be converted into half-space equivalent value using multiplier 2.

26

**(b)** Behind the loudspeaker at $z = -g$ there is an infinite impedance plane (substrate) as in previous chapters. Plane waves are absorbed at $z = \lambda_0$.

The absorbing boundary conditions are simply $\pm \frac{\partial P}{\partial z} - ik_0 P = 0$ in which the positive sign corresponds to a pressure wave propagating in positive $z$-direction [19].

Quality parameter $Q$ is an integer which represents the division of wire width $w$ into a discretized number of sources. Input Joule power per unit area is constant throughout the wire:

$$\frac{\bar{P}_J}{w N_w L_y} = -2i\omega C_s T(0) + \kappa(\partial_z T(0^-) - \partial_z T(0^+)) + \beta_0 T(0). \tag{88}$$

where $N_w$ is again the number of wires and $L_y$ is wire length. The second rectangular dimension of the loudspeaker is $L_x = dN_w$. Discretization of space must be done in a non-uniform way: In the proximity of the wire node separation follows $\lambda_T/32$-pattern. A smooth transition from thermal region into isentropic region is implemented and $z$-separation will eventually follow $\lambda_0/32$-pattern. For numerical accurary reasons, $x$-discretization is uniform and it is calculated using the $Q$-parameter. Node coordinates are defined in a recursive manner: After selecting $x$-displacement $\Delta x = w/Q$ and writing a table of $z$-displacements $\frac{\lambda_T}{32} \leq \Delta z_i \leq \frac{\lambda_0}{32}$, the following loops are executed:

$$x_i = i\Delta x, \ i \in \{1, 2, \ldots, N_x\} \tag{89}$$

$$z_{j+1} = z_j + \frac{\Delta z_{j+1} + \Delta z_j}{2}, \ j \in \{1, 2, \ldots, N_z - 1\} \tag{90}$$

where $N_x = Qd/w$ and $z_1 = 0$ (half-space) or $z_1 = -\lambda_0/2$ (full-space).

Discretization of the Laplacian operator $\nabla^2$ is done in the interior parts of the computational domain. For each interior node $(x_i, z_j)$ there are two linear thermoacoustic equations which follow from the time-harmonic PDEs (which are the oscillating parts extracted from Eqs. (21), (22))

$$\nabla^2 T + \frac{2i\omega}{\alpha} T + \frac{2i\omega}{\kappa} P = 0 \tag{91}$$

$$\nabla^2 P + k_P^2 P - \frac{4\omega^2 \rho_0}{T_0} T = 0. \tag{92}$$

The operator $\nabla^2$ is separated into two parts $\partial_x^2 + \partial_z^2$ in the cartesian domain. When operating on temperature at node $(i, j)$, the finite differences

approximation probes into four neighbouring nodes:

$$(\nabla^2 T)_{ij} \approx \frac{T_{i-1,j} - 2T_{ij} + T_{i+1,j}}{(\Delta x)^2}$$
$$+ \frac{2}{\Delta z_j} \left( \frac{T_{i,j-1} - T_{ij}}{\Delta z_{j-1} + \Delta z_j} - \frac{T_{ij} - T_{i,j+1}}{\Delta z_j + \Delta z_{j+1}} \right). \tag{93}$$

Periodic boundary conditions describe the interaction across $x$-boundaries: $T_{0,j} \equiv T_{Nx,j}$ and $T_{Nx+1,j} \equiv T_{1,j}$. The Laplacian of pressure has a similar form. The matrix structure of the linearized PDEs is sparse and banded. The field-theoretical aspects of the thermoacoustic problem fit into a $(2N \times 2N)$ linear equation system ($N = N_x N_z$ is total number of nodes). Boundary conditions are gathered together and the corresponding equations replace the empty rows of the PDE matrix. In Appendix 4 the construction of the linear equation system is carefully explained. One matrix inversion produces the vector of thermoacoustic nodal values which can be immediately visualized in the spatial domain. Only the real parts, phases and amplitudes of complex-valued temperature and pressure have physical meaning, though. Plane wave amplitude $P_0$ is readily obtained. Phase difference and amplitude of temperature on the wire surface can be averaged and plugged into Eq. (82). Total radiated acoustic power can be evaluated with the aid of Eqs. (15), (17), (86) and (87). In the calculations $|P(\varphi = 0, \theta = 0)|r_0$ must be replaced with $P_w R_0$ and loudspeaker area is $A = L_x L_y$.

## 4.4 Experimental methods

### 4.4.1 Principles of experimental acoustics

Traditionally all performance evaluations of loudspeakers are committed in anechoic free-field conditions. Previously, VTT loudspeakers has been studied in a so-called $2\pi$ anechoic room where the floor reflects acoustic waves [9]. In such a room it is possible to measure continuous waveforms reliably if the loudspeaker is placed on the floor pointing upwards. Experiments of this work were made in a normal, reverberant room where acoustic reflections formed an echo environment which disrupted the measurements. To achieve quasi-anechoic conditions, pressure sampling time was so short that no reflections could reach the microphone, and the selection of transmitted signals was therefore limited to bursts. For example, a few periods of sine waveforms could be transmitted at a single frequency. Maximum length sequences (MLS), which are more sophisticated bursts [22], were also generated. With the aid of MLS entire frequency bands could be studied at once. Responses were measured primarily in front of the loudspeakers on

28

the acoustic axis. Microphone was responsible for converting pressure wave into an electric signal from which amplitude and phase could be read. Input power is typically fixed to 1 W in acoustics, but the thermoacoustic speakers were driven with a wide range of electric powers in this work. In order to sample accurate off-axis responses at prescribed angles, the loudspeaker had to be mounted into an optical table. An example of experimental setup geometry is presented in Figure 5.
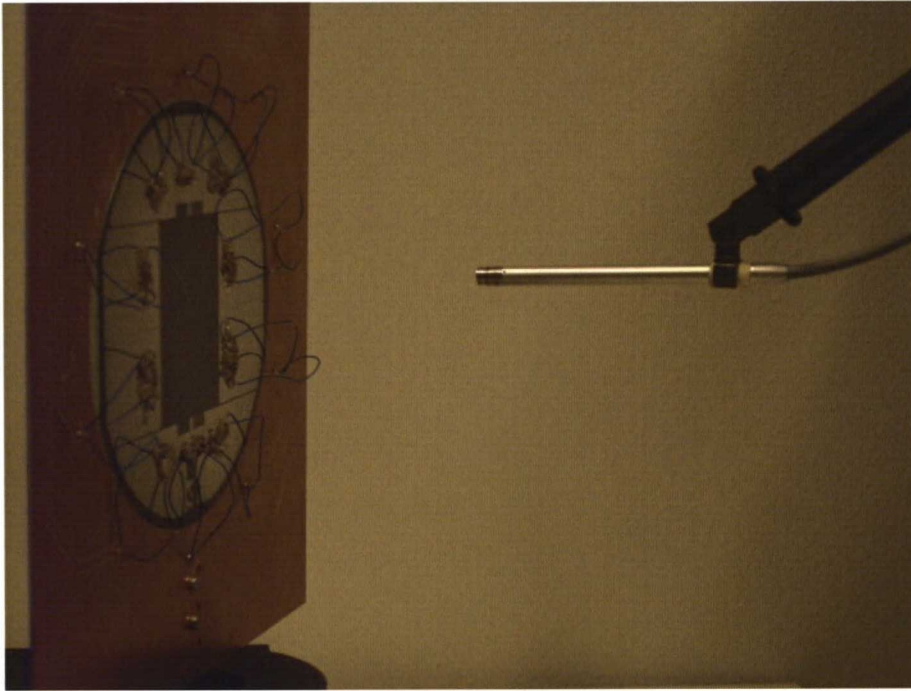


Figure 5: Near-field measurement setup

In the experiments of this work the audio transmitter consisted of

- Agilent 33220A arbitrary waveform generator
- DC power supply for providing bias voltage for MLS; Agilent E3631A was used among others
- Suspended thermoacoustic VTT loudspeaker on silicon wafer.

The function generator was fed with appropriate waveforms via PC interface. The audio receiver had the following parts:

29

- Brüel&Kjær (B&K) 4939 free-field microphone

- B&K 2670 pre-amplifier

- Stanford Research Systems SR560 pre-amplifier

- B&K Nexus 2690 conditioning amplifier

- Agilent 54832B Infiniium oscilloscope.

The B&K conditioning amplifier was responsible for generating a 200 V microphone polarization. The amplifier featured a second-order low-pass filter with 100 kHz corner frequency, so audio signal was amplified by the Stanford Research Systems pre-amplifier instead. The received waveforms were sampled with the Agilent oscilloscope and then forwarded to PC for post-processing.

### 4.4.2  Burst techniques

The loudspeaker response at a single frequency can be studied with repeated and averaged sine bursts. The burst interval should be so large that all transients die out before the next excitation is sent. Lower bound of frequency is set by the first reflection that arrives at the microphone. In other words, measuring sine amplitude would be impossible if line-of-sight signal and echo signal were separated by an interval shorter than the sine period. Averaging the received waveforms is a way to improve signal-to-noise ratio (SNR).

Maximum length sequence is a pseudo-random waveform that takes the values $\pm1$ [22]. The length of the sequence, which is $L = 2^n - 1$ where $n \geq 1$ is integer, must be chosen so that $L$ divided by receiver's sampling frequency $f_S$ is longer than impulse response (IR) of the loudspeaker. In a discrete, linear model the transmitted MLS signal is a sequence $u(n)$, $n \in \{0, 1, \ldots, L-1\}$ and the received signal is

$$y(n) = \sum_{k=0}^{M-1} h(k)u(n-k) + e(n), \ n \in \{0, 1, \ldots, M-1\} \tag{94}$$

where $h(k)$ is the accurate impulse response, $e(n)$ represents noise and $M$ is the number of received samples. The sum is a convolution which tells that the Fourier transform of $h$ is the frequency response of the loudspeaker. MLS has a peculiar autocorrelation property:

$$\sum_{n=0}^{L-1} u(n)u(n+m) = \begin{cases} L, & m = 0 \\ -1, & m \neq 0. \end{cases} \tag{95}$$

30

This suggests that IR can be estimated with the normalized cross-correlation of $u$ and $y$:

$$\bar{h}(m) = \frac{1}{L} \sum_{n=0}^{L-1} u(n)y(n+m), \ m \in \{0, 1, \ldots, M-1\}. \qquad (96)$$

After plugging in $y$, $\bar{h}$ appears to be slightly biased:

$$\bar{h}(m) = h(m) - \frac{1}{L} \sum_{k=0, k \neq m}^{M-1} h(k) + \frac{1}{L} \sum_{k=0}^{L-1} u(k)e(k+m). \qquad (97)$$

Time averages of $\bar{h}$ in the large-$L$ limit will converge to true IR provided that noise $e$ has zero mean. The superior SNR obtained with MLS excitations follows from the fact that cross-correlation of MLS and noise, which is present in equation (97), is almost always negligible [23].

In continuous time domain things get more complicated, though. The generation frequency $f_g$ of MLS blocks must be chosen carefully to match bandwidth and frequency resolution requirements. The power spectrum of a continuous MLS signal has sinc$^2$ profile with zeroes located at integer multiples of $f_g$. The first -3 dB point is approximately $f_g/3$ and the lower bound of frequency resolution is $f_g/L$. The sampling frequency $f_S$ of the receiver must be at least $f_g$ and, in agreement with Nyquist sampling theorem, $f_g/3$ must in turn be larger than doubled bandwidth of acoustic frequencies. [24]

# 5 Results

It was reasonable to begin acoustical measurements with a linearity check of loudspeaker operation. As explained in theoretical part of this work, output pressure $P_{rms}$ should be linearly proportional to average input power $\bar{P}_J$ in linear thermoacoustics. In the experiments, lower bound of frequency was set by the echo environment of measurement room and it was found to be in kHz range. For simplicity, sound frequency is $f = 2f_0$ in this chapter. In order to achieve a decent a signal-to-noise ratio, an input power larger than 0.2 W had to be generated. Upper bound of frequency was 150 kHz, the bandwidth of microphone calibration data sheet. Sine bursts with 20 periods were the first excitation signals used in measurements. Linearity check was done with loudspeaker C which was not biased with a DC signal. A self-made audio amplifier was utilized in the experiment: one passively cooled operation amplifier was connected in the non-inverting configuration. The circuit diagram is presented in Figure 6. The 35-$\Omega$ speaker was able
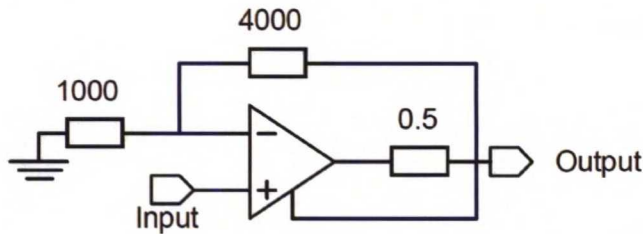
Figure 6: Operation amplifier Texas Instruments OPA541 in the non-inverting configuration. Resistances are shown in units of Ohms. DC power supplies $\pm V_S$, which are also connected in parallel to 10-$\mu$F capacitors, are not drawn. A fixed gain $G = 5$ was obtained from this device, but output current was limited to 1.6 A by the 0.5-$\Omega$ resistor.

to handle input powers in the range $\bar{P}_J = 0.5 - 10.5$ W while maintaining linearity (see Figure 7). The high-frequency artefacts were caused by resistance fluctuations of electric contacts on the wafer. Breakdown of individual wires and wire rows could be observed at higher input powers than 10.5 W. It is probable that the breakage is a thermal effect instead of being caused by high pressure amplitudes.

Complete far-field, on-axis responses of two loudspeakers were studied next. After collecting sine burst data at 7 cm distance from speaker B and at 19 cm distance from speaker E, MLS signals could be recorded at the same positions. In order to construct the shape of FR, the MLS procedure of previous chapter was followed. The absolute level of sound pressure level was
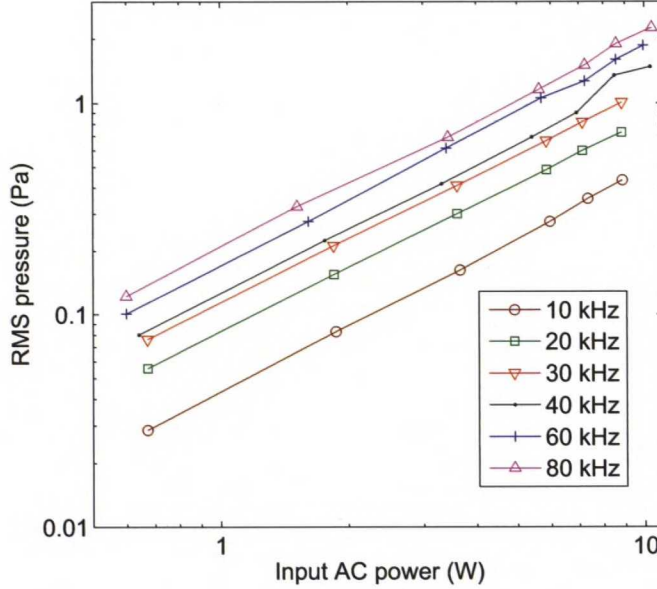
Figure 7: On-axis pressure response $P_{\mathrm{rms}}$ of speaker C at 7 cm distance as a function of input power $\bar{P}_J$ and sound frequency $f$. Microphone and pre-amplifier responses have not been cancelled out.

fixed with least squares fitting of MLS FR to point frequency SPLs of sine transmissions. MLS measurements were performed with a DC biased $15^{th}$ order signal of length $L = 32767$. In order to support the selected 150 kHz bandwidth, generation frequency was set to $f_g = 918$ kHz which corresponds to a 35.7-ms MLS period, much longer than the system's IR. Sampling frequency of the receiver was $f_S = 10$ MHz and theoretical lower bound of frequency resolution was 28 Hz. Received MLS and burst waveforms were pre-averaged during the measurement process.

Numerically solved thermoacoustic fields were immediately compared to measurements. The higher the frequency, the finer the computational mesh had to be due to shortening of wavelength. The upper bound of frequency was thus determined by available memory. The number of degrees of freedom, i.e., nodes in the mesh, can approach $10^6$ when directly solving linear equation systems on a 64-bit platform. A reasonable upper bound of complexity was found to be in the sub-MHz range. Sound radiation from 0.5 cm$^2$ loudspeaker B was calculated with all computational methods. In FEM simulations circular arrays of wires were defined in axisymmetric geometry with parameters $N_w = 133$ (number of wires) and $a = 3.99$ mm (array radius).

33

Heat capacity per unit area of a 30-nm layer of aluminium was $C_s = 0.0844$ J/(K·m²), and a generic value $\beta_0 = 25$ W/(K·m²) was used to represent auxiliary losses of wires in Eq. (64) [2]. The substrate was given a heat capacity per unit area $C_{s,Si}(\omega) = 16238 \cdot \omega^{-1/2}$ J·Hz$^{1/2}$/(K·m²) which follows from the insertion of high resistivity silicon properties into equations (41) and (42). Suspension parameter $g$ was fixed to 5 microns and all numerical parameters are listed in Appendix 1. Time-discretized and time-harmonic FEM solvers were compared against each other; the simulation principles were explained in chapters 4.3.2 and 4.3.3 of this work. Computing resources of CSC, the Finnish IT Center for Science, were utilized only when simulating the highest ultrasound frequencies; otherwise a desktop PC was capable of running the solvers. Sound pressure levels were sampled from pressure field solution vector $\xi_P$ (see equations (7) & (81) and Appendix 2). The results visible in Figure 8 did not essentially differ from each other which indicates that infinite elements were implemented correctly in the unbounded solver. Due to numerous advantages of the unbounded solver, such as availability of solution everywhere in half-space, there was no further need to perform slower time-discretized simulations.

FD simulation of a periodic array was implemented with $N_w = 167$ wires of length $L_y = 1$ cm (see the preceding chapter 4.3.4). The FD simulations were significantly faster to run and no external computing resources were needed. Array radius $a = 4$ mm was inserted into the formula (87) of Rayleigh distance $R_0$. Discretization quality was $Q = 11$ throughout the simulations. The pressure response has been plotted in Figure 8 and an excellent agreement with FEM results can be seen. Analytic ultimate limit of sound radiation has been plotted using Eq. (35) and the accompanying substrate correction (titled Finite impedance) from Eq. (45) agrees with FEM and FD in the low-frequency regime. It lacks the heat capacity correction which is essential in ultrasound range. Equation (62), which neglects loudspeaker sparsity, presents an exaggerated heat capacity correction (titled 1D model). According to Figure 8, the measurement results can be best explained with realistic FEM and FD simulations. For instance, in audible range of sound frequencies correct power law behaviour $P_{rms} \propto f^p$ with $p = 1.3 - 1.5$ was revealed. In ultrasound range $P_{rms}$ saturated and simulated SPL was $1 - 5$ dB higher than measured SPL. The SPL gap between analytic upper bound and speaker B response was always higher than 10 dB. Both FEM and FD simulations suffered from high condition numbers of the matrices that had to be inverted (see Appendices 2 & 3 and Eq. (81)). That is to say, iterative methods failed to converge due to the lack of numerical accuracy, and direct, time-consuming matrix inversion had to be performed. In fact, assembling the matrices was the most time-consuming part of the simulations. All FD simulations and audible-range FEM simulations at a single frequency could be completed within a couple of minutes. However, in the ultrasound range
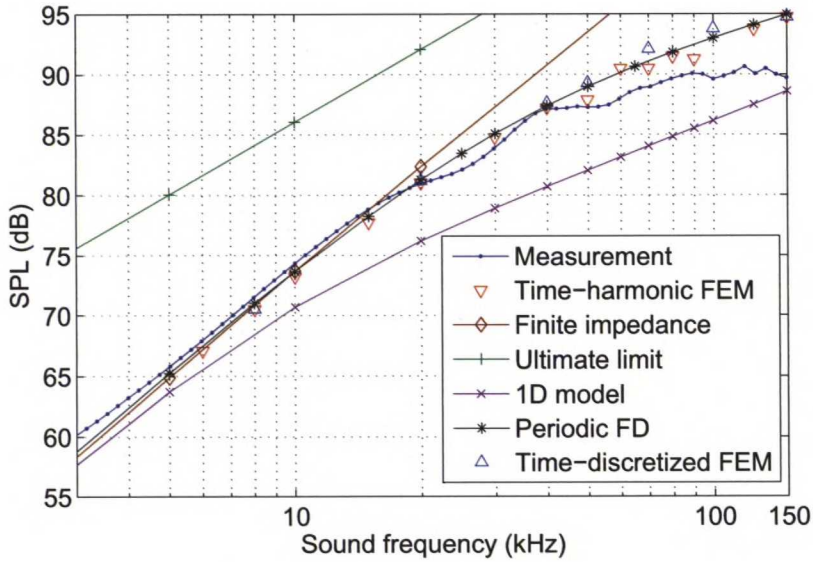
Figure 8: On-axis response of 1 cm × 0.5 cm speaker B at 7 cm distance and 1.2 W input power.

the FEM simulations could last for several hours.

Simulation of 17.5 cm$^2$ loudspeaker E with FEM required 787 wires and a 26.3-mm radius. Other computational methods were unaffected by the variation of loudspeaker size. As seen in Figure 9, the response in the audible range is congruent with loudspeaker B data in Figure 8: larger spatial dimensions have no influence on the on-axis pressure. However, the experimental response experiences a cut-off in ultrasound range which cannot be explained computationally. A possible cause could be the lack of perfect interference which may rotate the narrow main lobe of sound radiation. That is to say, the microphone was perhaps not measuring the exact on-axis response. Another plausible explanation could be the finite 1/4" diameter of the microphone diaphragm which may exceed the width of the radiation lobe.
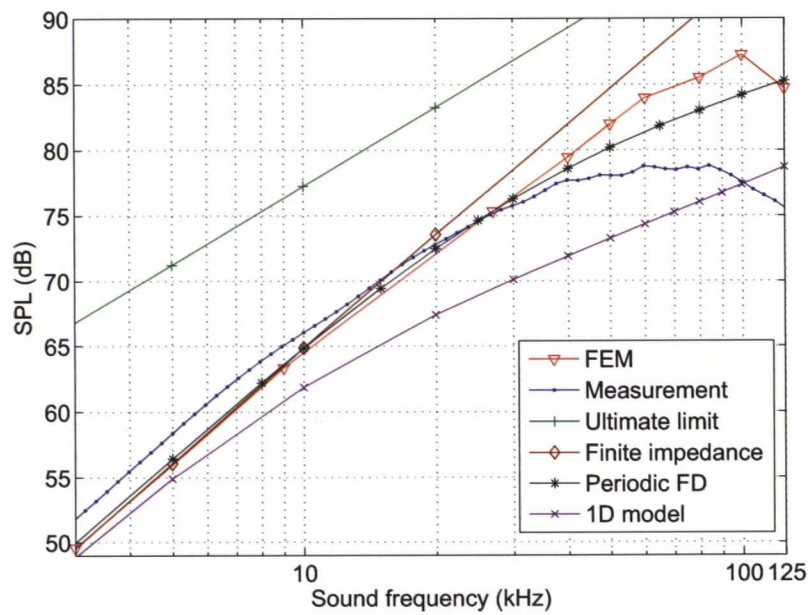
Figure 9: On-axis response of 3.5 cm × 5 cm speaker E at 19 cm distance and 1.2 W input power.

It was possible to displace the microphone into near-field and off-axis positions if input power of MLS transmissions was kept constant after the on-axis measurement. There was no need to search for new SPL calibration parameters. Spherical wave assumption in far field, $P_{\mathrm{rms}} \propto 1/r_0$, was validated using speaker A which has the same 0.5 cm$^2$ size as speaker B. As a result of raising $r_0$ from 7 cm to 17 cm, the shape of on-axis FR did not change but it experienced a $7 - 8$ dB downward shift (see Figure 10). The shift agreed well with the theoretical value $20 \log_{10}(7/17)$ dB $\approx$ -7.7 dB, and the shape of FR resembled the FR of speaker B in Figure 8. Next the loudspeaker was rotated with respect to the edge with length $L_x = 1$ cm. MLS waveforms were recorded at off-axis angles $\theta = 20°$ & $40°$. Testing the applicability of rectangular directivity function could be done by multiplying the on-axis response separately by $\mathrm{sinc}(k_0 L_x \sin(20°)/2)$ and $\mathrm{sinc}(k_0 L_x \sin(40°)/2)$ from equation (16). In Figure 10 it can be seen that the sinc-transform does indeed match the off-axis measurements. These results justify the use of equation
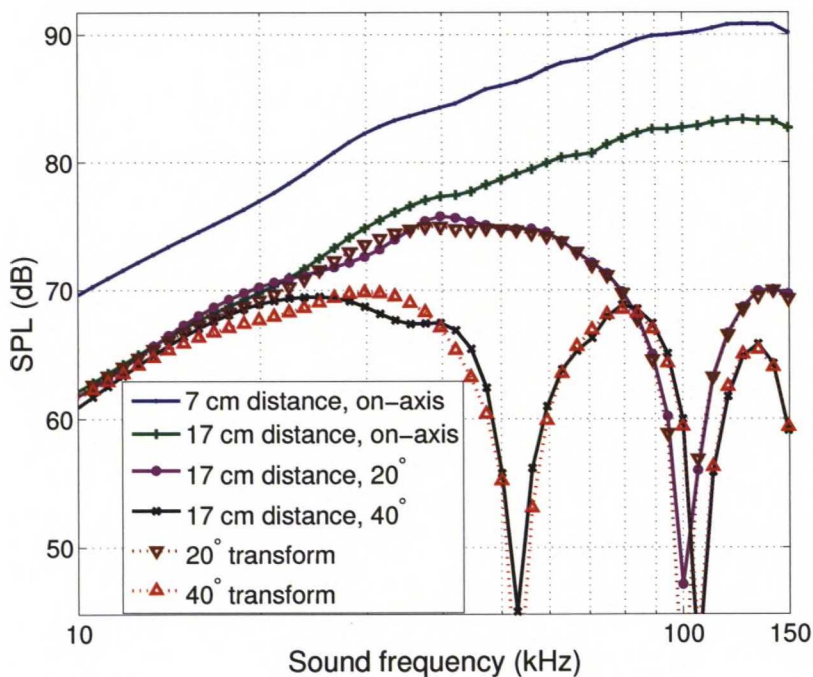


Figure 10: Measured frequency responses of 1 cm × 0.5 cm loudspeaker A with 1.2 W input power. Pressure spreads spherically in the shift from 7 cm to 17 cm. The speaker was rotated into off-axis angles 20° and 40° with respect to longer 1-cm edge. The off-axis responses are nicely found to follow the sinc-transform of Eq. (16).

37

(17) in the estimation of total radiated acoustic power. Experimental output power and FD simulation output power were obtained from on-axis pressure responses and in FEM simulations the sampling procedure of equation (84) was followed.

Next, loudspeaker optimization was studied computationally. Current photolithographic methods support the reduction of wire width to $w = 0.5 - 1.0$ $\mu$m. A threefold decrease of wire thickness is also within reach. Small 0.5 cm$^2$ loudspeakers were studied again with new thickness 10 nm and packing ratios 1/5 ($w = 1$ $\mu$m, $d = 5$ $\mu$m) & 1/20 ($w = 0.5$ $\mu$m, $d = 10$ $\mu$m). Another way of improving speaker efficiency is the complete removal of Si substrate. This was tested in standard (1/10) array geometry with both FEM and FD. Half-space data was obtained in FEM by raising gap $g$ above $\lambda_T$ which eliminates the acoustic contribution of the thermal boundary condition. Pressure waves reflected from the underlying plane gain a diminishingly small phase difference which has no notable effect. In full-space FD simulations, on the other hand, output pressure is simply doubled in order to achieve the half-space equivalent value of sound radiation.

Phase difference between Joule power and surface temperature is an indicator of the strength of the heat capacity effect. In FD solver it is straightforward to obtain both the phase $\bar{\phi}_w$ and amplitude $\bar{T}_w$ from averaged complex-valued temperature of $Q$ source points. In Figure 11 sparse loudspeakers are modelled with FD method and, for comparison purposes, the results of homogenous speakers (titled 1D models) are calculated using Eqs. (54) and (60). There is a striking deviation between homogenous and sparse free-standing (FS) loudspeakers. Of course, both phases approach $\pi/2$ in the limit of high frequency, but the phases differ by a factor of two in audible range of frequencies. Phases of sparse loudspeakers, FS and substrate-influenced, coincide eventually in ultrasound range which tells that the substrate has no thermoacoustic contribution anymore. The phase curve of homogenous, substrate-influenced loudspeaker shows that the phase can be strongly affected by a substrate. In Figure 12 additional optimization results are shown. The sparse and lossless loudspeaker shows a lower phase than $\pi/4$ which is the frequency-independent $\bar{\phi}_w$ of a homogenous loudspeaker in Eq. (54). Moreover, it can be deduced that the interplay between packing ratio, wire spacing and wire thickness determines the phase of lossy speakers. Thermoacoustic loudspeakers gain not only from absolute packing ratio, but also from the increase in wire spacing $d$. These both can effectively boost wire decoupling which begins when thermal wavelength $\lambda_T$ is as short as wire spacing. This results in thermal wave localization where surface temperature amplitudes are lower than in the wave overlap situation. This reduces the harmful amplitude of heat stored and released by $C_s$. Still, at low frequencies the wires show collective behaviour and the three phases in Figure 12
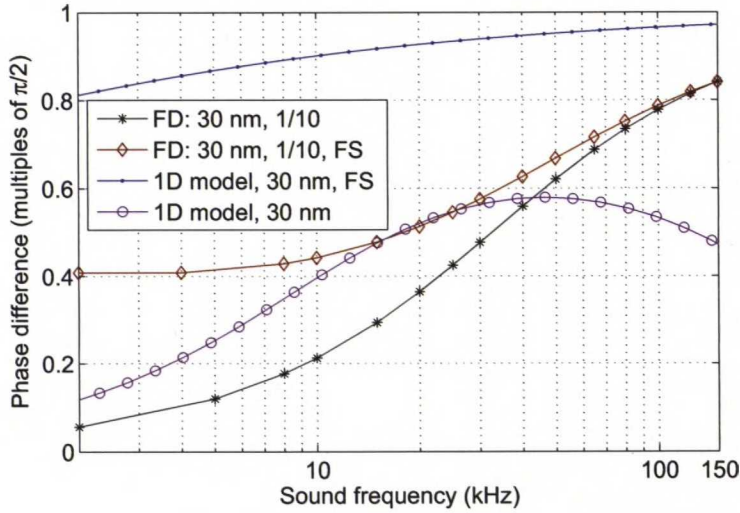
38

coincide.



Figure 11: Phase of surface temperature $\bar{\phi}_w$ in small, 30-nm thick loudspeakers. FS denotes free-standing speakers which are not affected by a substrate. Wire parameters $\beta_0$, $C_s$ are the same in all models. Packing ratio is $1/10$ in sparse loudspeakers while the 1D models represent homogenous speakers.
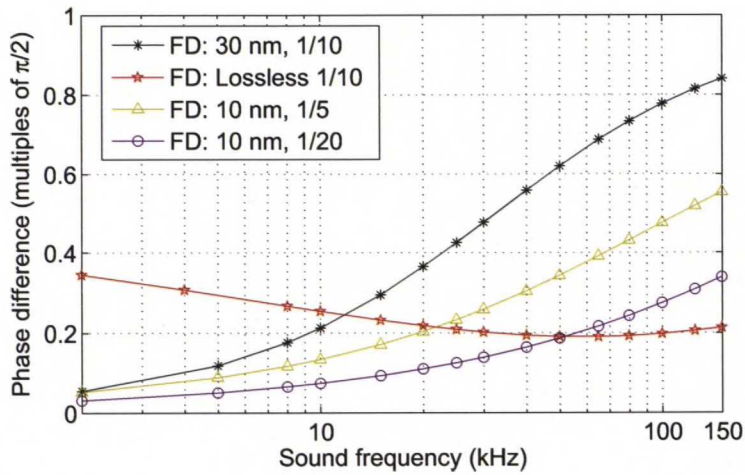


Figure 12: Phase of surface temperature $\bar{\phi}_w$ in small loudspeakers. Wire thicknesses and array packing ratios are shown. The lossless speaker is free-standing and its wire parameters $\beta_0$, $C_s$ are zero.

39

Estimates of acoustic efficiency have been gathered into Figure 13. In addition, in Figure 16 of Appendix 5 the efficiency data sets from FEM and FD are plotted simultaneously. They correspond well to each other but some numerical clutter is present in FEM results. It is likely to be caused by slight ill-conditioning of the field-theoretical problem. When source wires are lossy, emitted thermal power is dependent on wire temperature which is a piecewise linear function in half-space. Consequently, sound emission is affected by the size of the triangular finite elements inside which the point sources are located on $rz$-plane. For instance, too large finite elements lead into underestimation of surface temperature (especially when emitted thermal waves decay fast), and hence too high SPL. In the results of Figure 13, macroscopic loudspeaker size ($A = 0.5$ cm$^2$) leads into ultrasound interference effects which cause efficiency saturation or even cut-offs. The flat behaviour of the ultimate limit of efficiency reveals that $\eta \propto f^2$ thermoacoustic coupling is exactly compensated by directivity. This can be proven numerically by considering a directivity integral:

$$I_F = \frac{1}{2\pi} \int_0^{2\pi} \int_0^{\pi/2} \left( \frac{2J_1(k_0 a \sin\theta)}{k_0 a \sin\theta} \right)^2 \sin\theta d\theta d\varphi. \tag{98}$$

$I_F$ has been extracted from Eq. (17) and it decreases monotonically from omnidirectional radiation limit (unity) to zero as a function of frequency. It has a simple asymptotical form $I_F \approx 2/(k_0 a)^2 \propto f^{-2}$ in frequency range $f \geq f_c = c_0/(\pi a)$ that indeed explains the saturation of efficiency [25]. The corresponding efficiency maximum $\eta_c$ is

$$\eta(f \geq f_c) \approx \eta_c = \frac{\bar{P}_J c_0}{2A \rho_0 c_P^2 T_0^2}. \tag{99}$$

Sampled values of $\bar{T}_w$ and $\bar{\phi}_w$ were put into additional use in equations (82) and (85). Thermoacoustic efficiency $\eta_t$ was calculated without the contribution of $I_F$: this is the omnidirectionality assumption. The resulting curves in Figure 17 of Appendix 5 are thus depicting the $P$-$T$ coupling strength within the thin air slab next to the loudspeaker. Deviations from the ultimate limit are caused by the substrate, of course. The 1D model retrieves acoustic efficiency from Eq. (62) and the amplitude of thermal power is approximated with $P_{\text{air}} = |\bar{P}_J + 2i\omega A C_s T(g)|$. On the ultimate limit $P_{\text{air}} = \bar{P}_J$. An axisymmetric pressure field FEM solution has been drawn into Figure 14. The amplitude plot shows one main lobe and two side lobes of ultrasound radiation from a 0.5 cm$^2$ array. Near field is entirely enclosed by the computational domain of triangular finite elements. Lastly, temperature field near the wires is visualized in FD computational grid in Figure 15.
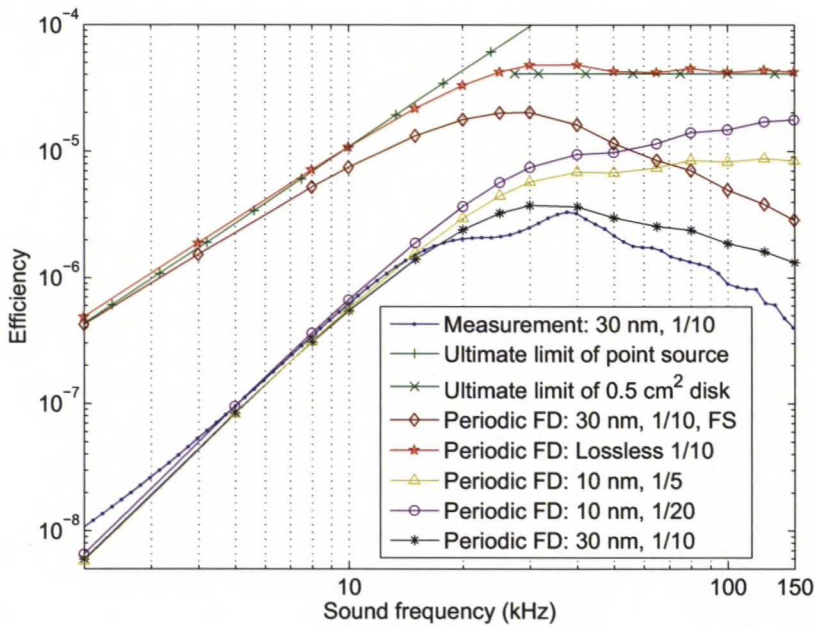
Figure 13: Acoustic efficiencies of a small loudspeaker with 1.2 W input electric power. Wire thicknesses and packing ratios are shown. FS is the free-standing mode where the substrate has been removed. In lossless mode wire parameters $\beta_0$, $C_s$ are set to zero as well.
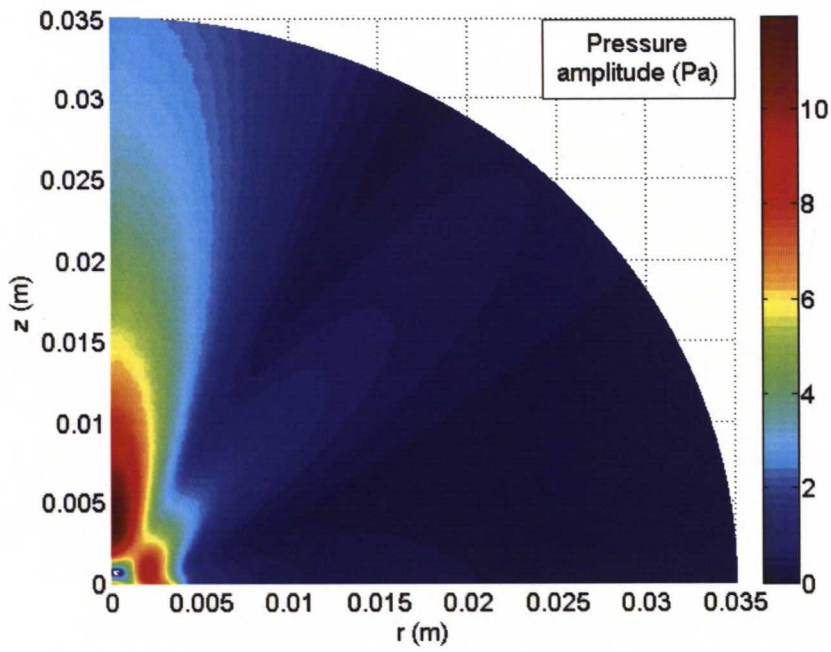
Figure 14: Oscillating pressure in near field (ultrasound amplitude at $f = 100$ kHz). The field was solved with time-harmonic FEM.
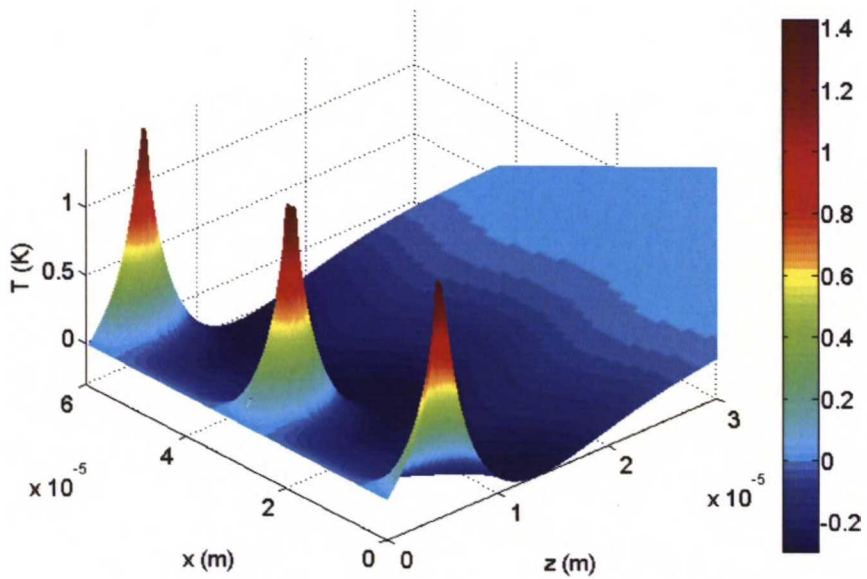
Figure 15: Oscillating temperature field in proximity to source wires (ultrasound frequency is $f = 100$ kHz). The field was solved using FD method with periodic boundary conditions and the single-wire solution has been drawn twice.

# 6  Conclusions

This work presented an overview of contemporary trends in thermoacoustic sound generation. For more than 100 years it was thought that thermoacoustics is not an attractive research topic because homogenous thin film loudspeakers had too low efficiency compared with piezoelectric transducers. All of a sudden in 2008, few-layer carbon nanotube (CNT) loudspeakers showed a remarkable decrease in the problematic heat capacity $C_s$ which limits the amplitude of thermal power emitted by a source resistor. CNT speakers were soon followed by metallic wire array loudspeakers designed by VTT. Even though the VTT speakers weren't free-standing, equally good thermoacoustic efficiency was measured. Two major improvements were introduced for the first time: (i) suspension provided an air gap which acts as superior insulator between source resistors and substrate; (ii) loudspeaker sparsity had a remarkably positive impact on ultrasound generation. In this work it was proved that modifying the sparsity of array loudspeakers is an excellent way of tuning the phase difference between input Joule power and heat released by $C_s$. Moreover, a long distance between wires in the array proved to be beneficial because the heat capacity effect is smaller when the wires are thermally decoupled.

Acoustic coupling factors, the square roots of efficiency, are presented in Table 1 for small VTT loudspeakers at universally adopted input electric power per sparse surface area 1 W/cm$^2$. Two reference values were found in literature. In 1999 sound was generated from a thin Al film on top of porous silicon: VTT loudspeaker B boasts a four times higher coupling factor. Still, the conventional electrodynamic method of sound generation cannot be surpassed by thermoacoustic means at audible frequencies. In ultrasound range,

Table 1: Acoustic coupling factors at 1 W/cm$^2$.

| Loudspeaker type | Maximal $\sqrt{\eta}$ ($10^{-3}$) | $f$ (kHz) |
|---|---|---|
| Speaker B: measurement | 1.18 | 38 |
| Speaker B: FD simulation | 1.19 | 35 |
| Speaker B: analytic upper bound | 4.45 | 35 |
| | Typical $\sqrt{\eta}$ ($10^{-3}$) | $f$ (kHz) |
| Thin film on porous silicon [10] | 0.3 | >10 |
| Conventional method [26] | 100 | ≤20 |

thermoacoustic loudspeakers are faced with competition againt piezoelectric transducers. While modern piezos are highly efficient, their frequency responses are peaked around a resonance frequency. Piezoelectric arrays may

44

sometimes show a wide-band frequency response, but crosstalk between individual transducers cannot be fully eliminated [27]. Thermoacoustic loudspeakers are, on the other hand, mediocre wide-band emitters as such. In addition, VTT wire arrays can be divided into subdomains which, when fed with signals with varying phase, can be made to radiate sound with custom directivity patterns. The simplest application could be user-defined ultrasound beamforming where the main lobe of radiation is freely rotated. Thermoacoustic loudspeakers gain also from the lack of moving parts: speaker structures could possibly be printed on paper as supplementary parts of larger circuits of printed electronics.

Ultimate efficiency of thermoacoustic sound generation was identified in this work. In linear field theory one can expect maximal loudspeaker efficiency to rise as a function of squared frequency until viscosity effects kick in at 1 GHz in standard conditions. In free field, omnidirectional spherical waves are energetically favourable. Directivity patterns of sound radiation, which typically arise from interference, impair acoustical intensity and total output power. Theoretical conclusions of this work suggest that an optimal thermoacoustic transducer is a wire array whose structure is a compromise between various geometric features. Maximal efficiency is inversely proportional to speaker surface area as seen in Eq. (99), but too small loudspeakers suffer from reduced power handling capacity. It is highly probable that DC heating effects are responsible for the breakdown of sound-emitting wires. What remains to be studied in future is maximal input power $\bar{P}_J$ that an $A$-sized loudspeaker with given thickness and packing ratio can reliably handle. Wire width is also a free optimization parameter here and together with thickness it determines the $C_s$ of a single wire.

In conclusion, thermoacoustic phenomenon is a weak, frequency-dependent and localized coupling effect which can be harnessed for sound generation. Two coupled partial differential equations of pressure and temperature give a sufficient mathematical description of linear thermoacoustics. In this work the PDEs were solved analytically under decoupling approximation, and it was possible to derive ultimate efficiency of sound radiation plus an accompanying impedance plane correction. The effect of a heat-absorbing substrate on VTT loudspeakers could be understood with impedance plane theory. In computer simulations the array loudspeakers were realistically modelled with FEM and FD solvers. The complicated thermophysical interplay between underlying substrate, array sparsity and wire heat capacity was studied, and numerical results were in good agreement with acoustic experiments. Thermoacoustic loudspeakers are unable to deliver high enough sound pressure levels for audible applications, but they have potential for some customized ultrasound applications. Generated sound waveforms are almost free of nonlinearities, pulsed loudspeaker operation is reliable, and no

structural resonance effects are found to emerge in the speakers.

## References

[1] H. D. Arnold and I. B. Crandall. The thermophone as a precision source of sound. *Phys. Rev.* **10**, 22-38 (1917).

[2] L. Xiao *et al.* Flexible, Stretchable, Transparent Carbon Nanotube Thin Film Loudspeakers. *Nano Lett.* **8**, 4539-4545 (2008).

[3] M. E. Kozlov *et al.* Sound of carbon nanotube assemblies. *J. Appl. Phys.* **106**, 124331 (2009).

[4] A. E. Aliev *et al.* Underwater Sound Generation Using Carbon Nanotube Projectors. *Nano Lett.* **10**, 2374-2380 (2010).

[5] F. A. McDonald and G. C. Wetsel, Jr. Generalized theory of the photoacoustic effect. *J. Appl. Phys.* **49**, 2313-2322 (1978).

[6] *Springer Handbook of Acoustics*, edited by T. D. Rossing (Springer 2007).

[7] V. Vesterinen. *Modelling a suspended thermoacoustic sound source.* Special Assignment in Acoustics and Audio Signal Processing (Aalto University 2010).

[8] D. T. Blackstock. *Fundamentals of physical acoustics* (John Wiley & Sons, Ltd. 2000).

[9] A. O. Niskanen *et al.* Suspended metal wire array as a thermoacoustic sound source. *Appl. Phys. Lett.* **95**, 163102 (2009).

[10] H. Shinoda *et al.* Thermally induced ultrasonic emission from porous silicon. *Nature* **400**, 853-855 (1999).

[11] B. Gelloz, M. Sugawara and N. Koshida. Acoustic Wave Manipulation by Phased Operation of Two-dimensionally Arrayed Nanocrystalline Silicon Ultrasonic Emitters. *Jpn. J. Appl. Phys.* **47**, 3123-3126 (2008).

[12] H. Hu, T. Zhu, and J. Xu. Model for thermoacoustic emission from solids. *Appl. Phys. Lett.* **96**, 214101 (2010).

[13] R. R. Boullosa and A. O. Santillan. Ultrasonic Radiation from Simple Thermoacoustic Transducers. *Acta Acust. Acust.* **90**, 277-284 (2004).

[14] D. R. Penn. Electron mean-free-path calculations using a model dielectric function. *Phys. Rev. B* **35**, 482-486 (1987).

[15] M. Ochmann and H. Brick. Acoustical Radiation and Scattering above an Impedance Plane. In *Computational Acoustics of Noise Propagation in Fluids - Finite and Boundary Element Methods*, edited by S. Marburg and B. Nolte (Springer 2008).

[16] M. Ochmann. The Complex Equivalent Source Method for Sound Propagation over an Impedance Plane. *J. Acoust. Soc. Am.* **116**, 3304-3311 (2004).

[17] A. Sommerfeld. *Partial Differential Equations in Physics* (Academic Press, New York 1949).

[18] H. D. Baehr and K. Stephan. *Heat and Mass Transfer*, $2^{nd}$ edition (Springer 2006).

[19] B. Alpert, L. Greengard and T. Hagstrom. Nonreflecting Boundary Conditions for the Time-dependent Wave Equation. *J. Comp. Phys.* **180**, 270-296 (2002).

[20] P. Solin. *Partial Differential Equations and the Finite Element Method* (John Wiley & Sons, Inc. 2006).

[21] R. J. Astley. Mapped Spheroidal Wave-envelope Elements. *Int. J. Numer. Meth. Engng.*, **41**, 1235-1254 (1998).

[22] P. M. S. Burt. Measuring Acoustic Responses with Maximum-length Sequences. Telecommunications Symposium, 1998, *ITS'98 Proceedings* (IEEE).

[23] G.-B. Stan, J.-J. Embrechts and D. Archambeau. Comparison of Different Impulse Response Measurement Techniques. *J. Audio Eng. Soc.* **50**, 249-262 (2002).

[24] M. Vilkko and T. Roinila. *Designing Maximum Length Sequence Signal for Frequency Response Measurement of Switched Mode Converters*. Nordic Workshop on Power and Industrial Electronics, June 9-11, 2008.

[25] V. Vesterinen, A. O. Niskanen, J. Hassel, and P. Helistö. Fundamental Efficiency of Nanothermophones: Modeling and Experiments. *Nano Lett., in press* (2010); See also the Supplementary materials.

[26] R. Venkatasubramanian. Nanothermal trumpets. *Nature* **463**, 619 (2010).

[27] R. L. Goldberg and S. W. Smith. Multilayer Piezoelectric Ceramics for Two-Dimensional Array Transducers. *IEEE Trans. Ultrasonics Ferroelectr Freq. Control* **41**, 761-771 (1994).

[28] E. Sanmiguel-Rojas, J. Ortega-Casanova, C. del Pino, and R. Fernandez-Feria. A Cartesian grid finite-difference method for 2D incompressible viscous flows in irregular geometries. *J. Comp. Phys.* **204**, 302-318 (2005).

Table 2: **Appendix 1**. List of constants and parameters used.

| Symbol | Name | (Value and) Unit | Notes |
|---|---|---|---|
| $\alpha$ | Diffusion constant | $2.25 \cdot 10^{-5}\ \frac{m^2}{s}$ | Air at 300 K temperature |
| $\beta_0,\ \beta_{0,Si}$ | Rate of heat loss per unit area and unit rise in temperature | $25\ \frac{W}{K \cdot m^2}$ | Thin film result in Ref. [2] |
| $c_0$ | Isentropic speed of sound | $344\ \frac{m}{s}$ | Air at 300 K |
| $c_P$ | Specific heat of air | $1007\ \frac{J}{kg \cdot K}$ | Constant pressure and 300 K temperature |
| $C_s$ | Heat capacity per unit area of wire | $0.0844\ \frac{J}{K \cdot m^2}$ | Aluminum at 300 K, thickness 30 nm |
| $\kappa$ | Heat conductivity | $2.63 \cdot 10^{-2}\ \frac{W}{K \cdot m}$ | Air at 300 K |
| $P_0$ | Ambient pressure | 1 atm | |
| $\rho_0$ | Density | $1.16\ \frac{kg}{m^3}$ | Air at 300 K |
| $T_0$ | Ambient temperature of air | 300 K | Room temperature |
| $\alpha_{Si}$ | Diffusion constant of silicon | $9.588 \cdot 10^{-5}\ \frac{m^2}{s}$ | At 300 K temperature |
| $C_{Si}$ | Heat capacity per unit volume of silicon | $1.16 \cdot 10^6\ \frac{J}{m^3 \cdot K}$ | At 300 K temperature |
| $C_{s,Si}$ | Heat capacity per unit area of silicon | $\frac{J}{K \cdot m^2}$ | At 300 K temperature |
| $g$ | Air gap parameter | $5\ \mu m$ | Distance between sound source and substrate |
| $a$ | Radius of circular array | 0.399 cm | Surface area 0.5 cm$^2$ |
| | | 2.360 cm | Surface area 17.5 cm$^2$ |
| $\eta = P_{\text{ac}}/\bar{P}_J$ | Loudspeaker efficiency | | |
| $f = 2f_0$ | Sound frequency | Hz | |
| $L_x, L_y$ | Rectangular dimensions | 0.5 cm × 1.0 cm | Speakers A, B and C |
| | | 3.5 cm × 5.0 cm | Speaker E |
| $\omega = 2\pi f_0$ | Angular frequency of voltage | rad/s | |
| $P_{\text{ac}}$ | Average acoustic power | W | |
| $\bar{P}_J$ | Average electric power | W | |
| $r_0$ | Distance from loudspeaker | cm | |

## Appendix 2: Time discretization of linear equation system.

Crank-Nicholson time discretization is performed here for linear systems (71) and (72). Physical quantities $P$, $T$, $X$ and $Y$ are calculated on time step $n+1$ using matrix inversion and data from step $n$. First a coupled system of size $2N$ is formed: on left hand side there should be a constant matrix times vectors $\xi_X^{n+1}$ and $\xi_Y^{n+1}$. On right hand side no vector should be unknown.

The coupled system will look like

$$B_1 \begin{pmatrix} \xi_X^{n+1} \\ \xi_Y^{n+1} \end{pmatrix} = B_2 \begin{pmatrix} \xi_X^n \\ \xi_Y^n \end{pmatrix} - B_3 \xi_P^n + B_4(\dot{P}_J^{n+1} + \dot{P}_J^n) \tag{100}$$

where

$$B_1 = \begin{pmatrix} \frac{1}{\Delta t}M + \frac{\alpha c_0^2}{2c_T^2}\hat{S} + \frac{\alpha C_{s,Si}c_0^2}{\kappa c_T^2 \Delta t}M_3 + \frac{\alpha c_0^2}{2\pi\kappa c_T^2}\left(\frac{\beta_0}{2} + \frac{C_s}{\Delta t}\right)M_w & \frac{\alpha c_0^2 \Delta t}{4\kappa}\hat{S} \\ -\frac{\rho_0}{T_0}M & \frac{1}{c_T^2}M + \frac{\Delta t^2}{4}\hat{S} + \left(\frac{\Delta t}{2c_0} + \frac{\Delta t^2}{4b}\right)M_2 \end{pmatrix} \tag{101}$$

$$B_2 = \begin{pmatrix} \frac{1}{\Delta t}M - \frac{\alpha c_0^2}{2c_T^2}\hat{S} + \frac{\alpha C_{s,Si}c_0^2}{\kappa c_T^2 \Delta t}M_3 + \frac{\alpha c_0^2}{2\pi\kappa c_T^2}\left(-\frac{\beta_0}{2} + \frac{C_s}{\Delta t}\right)M_w & -\frac{\alpha c_0^2 \Delta t}{4\kappa}\hat{S} \\ -\frac{\rho_0}{T_0}M & \frac{1}{c_T^2}M - \frac{\Delta t^2}{4}\hat{S} - \left(\frac{\Delta t}{2c_0} + \frac{\Delta t^2}{4b}\right)M_2 \end{pmatrix} \tag{102}$$

$$B_3 = \begin{pmatrix} \frac{\alpha c_0^2}{\kappa}\hat{S} \\ \Delta t\hat{S} + \frac{\Delta t}{b}M_2 \end{pmatrix} \tag{103}$$

and

$$B_4 = \begin{pmatrix} \frac{\alpha c_0^2}{4\pi\kappa c_T^2}b_w \\ 0 \end{pmatrix} \tag{104}$$

Dirichlet boundary conditions on $\Gamma_2$ have yet to be placed on the upper half of the large system. It can be seen that electric powers $\dot{P}_J^n$ can be arbitrary and many kinds of loudspeaker responses can be studied. Stationary component of electric power becomes irrelevant, though. This simulation model is not capable of solving the steady-state temperature field.

Matrix $B_1$ is unsymmetrical but invertible, so vectors $\xi_X^{n+1}$ and $\xi_Y^{n+1}$ can be solved and plugged into

$$\begin{pmatrix} \xi_T^{n+1} \\ \xi_P^{n+1} \end{pmatrix} = \begin{pmatrix} \xi_T^n \\ \xi_P^n \end{pmatrix} + \frac{\Delta t}{2}\begin{pmatrix} \xi_X^{n+1} + \xi_X^n \\ \xi_Y^{n+1} + \xi_Y^n \end{pmatrix}, \tag{105}$$

and thermoacoustic fields can be visualized at every time step if necessary.

## Appendix 3: Finite element matrices the infinite domain.

Mass and stiffness matrices become more complicated in quadrilateral infinite elements $Q$ [21]. An element of local mass matrix will look like

$$(M_r)_{ij} = \int_Q D(r,z) P_i(r,z) P_j(r,z) r dr dz \qquad (106)$$

where $P_i$:s are piecewise continuous polynomial shape functions. Function $D$ is defined later. An element of local stiffness matrix, $(\hat{S}_r)_{ij}$, is sum of five integral contributions:

1. $\int_Q P_i (\nabla D \cdot \nabla P_j) r dr dz$

2. $-ik_0 \int_Q P_i P_j (\nabla D \cdot \nabla \mu) r dr dz$

3. $\int_Q D(\nabla P_i \cdot \nabla P_j) r dr dz$

4. $ik_0 \int_Q [D(P_i \nabla P_j - P_j \nabla P_i) \cdot \nabla \mu] r dr dz$

5. $k_0^2 \int_Q D P_i P_j |\nabla \mu|^2 r dr dz$.

It should be noted that the quadrilateral elements comprise several node pairs. A pair is located at a desired distance from origin and $\Gamma_2$. In addition, for all the nodes on left (right) edge, $\theta_1$ ($\theta_2$) $= \arctan(r/z)$ is constant. A clever coordinate transformation can be performed: the idea is that integrals over element $Q$ on $rz$-plane will be evaluated in a square reference element on $uv$-plane. The transformation $(r,z) = F(u,v)$ has a form

$$\begin{pmatrix} r \\ z \end{pmatrix} = \frac{2b}{1-v} \begin{pmatrix} \sin \alpha(u) \\ \cos \alpha(u) \end{pmatrix} \qquad (107)$$

where $b$ is distance from origin to $\Gamma_2$ and

$$\alpha(u) = \frac{\theta_1}{2}(1-u) + \frac{\theta_2}{2}(1+u). \qquad (108)$$

The reference square is centered at origin of $uv$-plane and it has edge length 2. End points $u = \pm 1$ represent left and right edges of the infinite element while $v = \pm 1$ represent $\Gamma_2$ and infinity, respectively. Finding $D$ and $\mu$ is a straightforward task in $uv$-plane:

$$D = \left( \frac{1-v}{2} \right)^2 = \frac{b^2}{r^2 + z^2} \quad \& \quad \mu = b \left( \frac{1+v}{1-v} \right) = \sqrt{r^2 + z^2} - b. \qquad (109)$$

## Appendix 4: Finite differences method: Linear equation system.

An interior node $(i,j)$ of discretized $xz$-domain gives rise to two thermoacoustic equations

$$(\nabla^2 T)_{ij} + \frac{2i\omega}{\alpha} T_{ij} - \frac{2i\omega}{\kappa} P_{ij} = 0 \tag{110}$$

$$(\nabla^2 P)_{ij} + k_P^2 P_{ij} - \frac{4\omega^2 \rho_0}{T_0} T_{ij} = 0 \tag{111}$$

where the Laplacian operator $\nabla^2$ may contain interaction between boundary nodes $(1,j)$ and $(N_x, j)$ (see Eq. 93). Plane waves which propagate in positive $z$-direction are absorbed using

$$pP_{i,Nz-2} + mP_{i,Nz-1} + (s - ik_0)P_{i,Nz} = 0 \tag{112}$$
$$pT_{i,Nz-2} + mT_{i,Nz-1} + (s - ik_0)T_{i,Nz} = 0 \tag{113}$$

where $p$, $m$ and $s$ are the constants of a two-point first-order derivative (see Ref. [28]). The weak temperature wave is also isentropic. On the opposite $z$-boundary there are either impedance boundary conditions (in half-space)

$$P_{i,1} - P_{i,2} = 0 \tag{114}$$
$$pT_{i,3} + nT_{i,2} + (s + 2i\omega C_{s,Si}/\kappa)T_{i,1} = 0 \tag{115}$$

or wave absorptions (in full-space)

$$pP_{i,3} + nP_{i,2} + (s + ik_0)P_{i,1} = 0 \tag{116}$$
$$pT_{i,3} + nT_{i,2} + (s + ik_0)T_{i,1} = 0. \tag{117}$$

The definition of constant $n$ is in Ref. [28]. Finally, Joule power source equations are

$$P_{i,Ng} - P_{i,Ng+1} = 0 \tag{118}$$

$$-\frac{\kappa}{\Delta z}T_{i,Ng-1} + \left(\frac{2\kappa}{\Delta z} - 2i\omega C_s + \beta_0\right)T_{i,Ng}$$

$$-\frac{\kappa}{\Delta z}T_{i,Ng+1} = \frac{\bar{P}_J}{wN_w L_y} \tag{119}$$

where $i \in \{1, \ldots, Q\}$ and $j = N_g$ corresponds to $z = 0$ around which $z$-discretization is locally uniform ($\Delta z_{Ng} = \Delta z_{Ng\pm1} = \Delta z$).
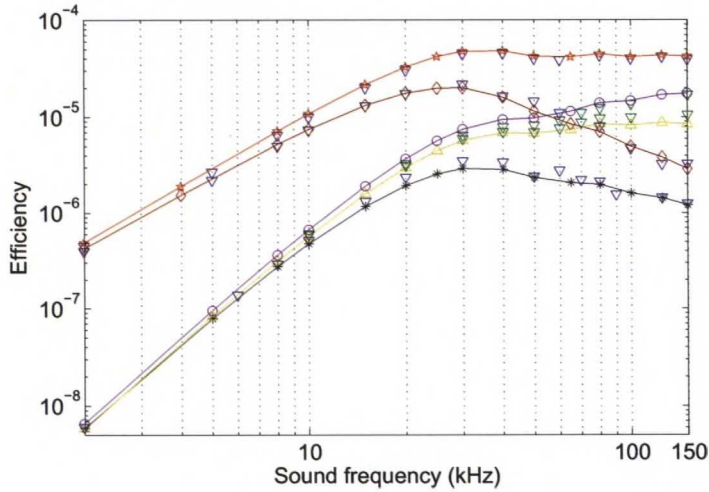
## Appendix 5: Supplementary figures.



Figure 16: Comparison of acoustic efficiencies calculated with FEM and FD in similar situations. Inverted triangles represent FEM data points, and FD curves have been copied from Figure 13.
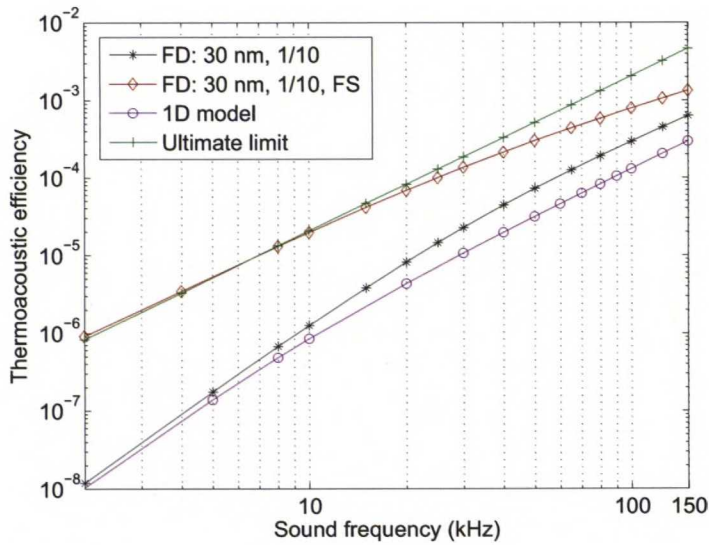


Figure 17: Thermoacoustic efficiencies of a small loudspeaker with 1.2 W input electric power. Directivity effects have been cancelled out: all curves represent radiation from a point source. FS is again the free-standing mode.